Characterising the response of vegetation cover to water limitation in Africa using geostationary satellites

Çağlar Küçük [1,2], Sujan Koirala [1], Nuno Carvalhais [1,3], Diego G. Miralles [2], Markus Reichstein [1], Martin Jung [1]

[1]Department of Biogeochemical Integration, Max Planck Institute for Biogeochemistry, Jena, Germany
[2]Hydro-Climate Extremes Lab (H-CEL), Faculty of Bioscience Engineering, Ghent University, Ghent, Belgium
[3]CENSE, Departamento de Ciências e Engenharia do Ambiente, Faculdade de Ciências e Tecnologia, Universidade NOVA de Lisboa, Caparica, Portugal

Key Points:

- We detect seasonal decay periods of fractional vegetation cover at Africa from daily geostationary satellite time series at 5 km resolution
- We provide observation-based metrics characterising dynamics of decay periods to improve our understanding in vegetation–water interactions
- The metrics contain valuable information on underlying processes of decay related to water limitation like plant accessible water storage

Corresponding author: Çağlar Küçük, ckucuk@bgc-jena.mpg.de

Abstract

Hydrological interactions between vegetation, soil, and topography are complex, and heterogeneous in semi-arid landscapes. This along with data scarcity poses challenges for large-scale modelling of vegetation-water interactions.

Here, we exploit metrics derived from daily Meteosat data over Africa at ca. 5 km spatial resolution for ecohydrological analysis. Their spatial patterns are based on Fractional Vegetation Cover (FVC) time series and emphasise limiting conditions of the seasonal wet to dry transition: the minimum and maximum FVC of temporal record, the FVC decay rate and the FVC integral over the decay period. We investigate the relevance of these metrics for large scale ecohydrological studies by assessing their co-variation with soil moisture, and with topographic, soil, and vegetation factors.

Consistent with our initial hypothesis, FVC minimum and maximum increase with soil moisture, while the FVC integral and decay rate peak at intermediate soil moisture. We find evidence for the relevance of topographic moisture variations in arid regions, which, counter-intuitively, is detectable in the maximum but not in the minimum FVC. We find no clear evidence for wide-spread occurrence of the "inverse texture effect" on FVC. The FVC integral over the decay period correlates with independent data sets of plant water storage capacity or rooting depth while correlations increase with aridity. In arid regions, the FVC decay rate decreases with canopy height and tree cover fraction as expected for ecosystems with a more conservative water-use strategy. Thus, our observation-based products have large potential for better understanding complex vegetation–water interactions from regional to continental scales.

Plain Language Summary

Local-scale processes controlling vegetation dynamics under water limitation are highly uncertain at large scales, despite their importance on global carbon and water cycles. This is particularly pronounced in Africa due to the scarcity of ground measurements despite the importance of African ecosystems due to their contribution to global cycles and their services to population. In order to overcome this problem, we developed a set of metrics based on the fractional vegetation cover observed from the European geostationary satellite. The metrics help diagnose the effects of local-scale ecohydrological processes thanks to their high spatial resolution of ca. 5 km. Initial analyses show consistent continental gradients in the metrics together with strong local variations and corroboration with different datasets from independent sources, in agreement with the literature.

1 Introduction

Africa hosts the largest share of undernourished population, and the livelihood of the majority of its population relies on ecosystem services and water availability (Müller et al., 2014). Moreover, African ecosystems contribute strongly to fluctuations of the global carbon cycle (Williams et al., 2007; Weber et al., 2009; Valentini et al., 2014; Palmer et al., 2019). Despite its importance, large uncertainties prevail in understanding the African ecosystems and quantifying spatiotemporal variations of their functioning due to the complexity of continental gradient and scarcity of ground measurements, which has been shown in studies using different data and approaches ranging from in-situ observations (Schmiedel et al., 2021), over remote sensing (Weerasinghe et al., 2020), to ecosystem modelling (C. Martens et al., 2021), as well as systematic literature reviews (Adole et al., 2016).

Savannas cover majority of the African continent (Williams & Albertson, 2004), and water is the limiting factor in such ecosystems, affecting vegetation's carbon uptake and nitrogen assimilation (Rodríguez-Iturbe et al., 1999). The dominant role of water

in African drylands has been shown in various studies (Sankaran et al., 2005, 2008; Merbold et al., 2009; F. Wei et al., 2019). Moreover, evidence suggests that ecosystem functioning – even in the wettest part of the continent, the central African tropical forest – responds to soil moisture fluctuations (Guan et al., 2013; Gond et al., 2013) along with co-limitations of other factors such as radiation (Adole et al., 2019). Within the complex rainfall seasonality patterns having unimodal, bimodal or trimodal regimes, less than 5 % of the continent is reported to be non-seasonally humid (Herrmann & Mohr, 2011).

Soil moisture is the critical variable that characterises the water limitation of vegetation (Porporato et al., 2001), which, in turn, shapes land–atmosphere exchanges of carbon, water, and energy fluxes (Gentine et al., 2012), phenology (Peñuelas et al., 2004), and vegetation functional traits (Guan et al., 2015; W. Zhang et al., 2019), along with their species or biome distribution (Xu et al., 2016). Rainfall is the primary source of moisture but plant available water in drylands is characterised by non-trivial and complex ecohydrological processes that control the availability of moisture from secondary sources (D'Odorico et al., 2019). In fact, Wilcox et al. (2017) conceptualised three critical ecohydrological junctures: (1) infiltration versus overland flow, (2) soil evaporation versus transpiration, and (3) root water uptake versus drainage, that are all centred around the hydrological response of the ecosystem.

Beyond precipitation intensity, topography, and soil properties, the first juncture is affected by presence of vegetation patches that interact with overland flow causing the typical runoff–runon dynamics at hillslope-scale (Ludwig et al., 2005). The second juncture, partitioning of terrestrial evaporation, is critical as an interplay between biological activity and productivity, and physical water losses by direct evaporation. Vegetation transpiration generally dominates terrestrial evaporation (Z. Wei et al., 2017), and the partitioning is controlled more by vegetation and soil characteristics given the climate (Nelson et al., 2020), highlighting a pivotal role of vegetation. The third juncture within the root zone is largely controlled by below-ground vegetation properties, such as depth and distribution of roots, that control the soil–plant hydraulics continuum. Deep rooting facilitates access to a larger moisture reservoir, a frequently observed trait in savanna and woodland ecosystems (Kleidon & Heimann, 1998; Guswa, 2008). In fact, the diversity and complementarity of ecohydrological plant traits by different species within ecosystems was shown to determine resilience to drought (Anderegg et al., 2018) and to maximise plant water use (Scanlon et al., 2005; Caylor et al., 2009).

There are further ecohydrological phenomena that should be considered when exploring vegetation–water interactions, emerging from non-monotonic ecosystem responses to episodic events, and ephemeral waterbodies occurring across spatial scales. Non-monotonic effects of soil properties on the interaction between climatological aridity and vegetation can lead to the frequently observed "inverse texture effect" in arid climates, whereby sandy soils appear to be associated with less water stress compared to clay soils, due to their higher infiltration capacity (Noy-Meir, 1973). Additionally, dryland ecosystems locally return nearly all rainfall back to atmosphere as terrestrial evaporation (Newman et al., 2006) with very little water draining from the root zone to groundwater (Wilcox et al., 2017), except extreme rainfall events that episodically recharge aquifers (Taylor et al., 2013; J. Zhang et al., 2016). Moreover, riparian processes such as river channel losses from ephemeral rivers can provide critical source of moisture (Tooth, 2000; Mansell & Hussey, 2005; Jacobson & Jacobson, 2013; Wang et al., 2018). Riparian corridors and groundwater-fed valleys, therefore, often appear as "green islands" (Eamus et al., 2015), where access to the shallow groundwater supports vegetation activities. In such ecosystems, the growing season may continue several months after the rain season has ceased while the trees appear to have access to groundwater via deep roots or recharge their trunks with water during these times (Guan, Wood, et al., 2014; F. Tian et al., 2018).

Previous studies, therefore, provide clear evidence that vegetation functions are controlled by moisture availability in non-humid climate, with moisture availability, itself,

emerging from the complex interplay among climate characteristics, vegetation traits, hillslope topography, soil properties, and presence of secondary moisture sources, e.g., aquifers. In fact, incorporation of all these ecohydrological factors poses a challenge for land-surface modellers (Clark et al., 2015; Fisher & Koven, 2020). One of the main limitations for models is the specification of rooting depth (Fan et al., 2019). Over recent years, several studies have put forward estimations of the rooting depth or effective rooting depth that represents the potential moisture access of the vegetation. A comparison of different estimates, though, reveals a large uncertainty with rooting depth varying from a few centimetres to tens of meters for a given location (Wang-Erlandsson et al., 2016). This, in part, is caused by the underlying assumptions in the estimation methods, whose effect on the prediction cannot be constrained by or validated against observations, especially in data scarce regions like Africa. Considering the particular difficulties associated with below-ground observation of ecosystem and land properties at a large-scale, remotely-sensed products of vegetation characteristics, indices, and responses provide opportunities to back infer the underlying environmental factors and land surface characteristics.

Remote sensing vegetation indices has been extensively used to capture phenological states of vegetation, such as detecting onset and length of growing season or peak greenness, as well as specific agricultural applications (reviewed in Zeng et al., 2020). Moreover, the temporal dynamics of vegetation indices can be exploited to understand ecologically relevant concepts such as land cover effects on vegetation dynamics (Yan et al., 2017), early green-up of woody vegetation in Africa (Guan, Wood, et al., 2014; Adole et al., 2019; Ouédraogo et al., 2020), effects of plant water storage (F. Tian et al., 2018), and early diagnosis of climate-induced forest mortality (Liu et al., 2019). The majority of vegetation remote sensing studies focusing on Africa are based on image acquisitions from polar orbiting satellites like MODIS (Adole et al., 2016), while only a few studies are based on vegetation indices derived from the geostationary satellite Meteosat Second Generation (MSG) (e.g.: Guan, Medvigy, et al., 2014; Yan et al., 2017). Geostationary satellite based vegetation indices are available in daily temporal resolution, which is their biggest advantage compared to polar orbiting satellites where such high resolution in time is not possible.

In this study, we analyse the daily Fraction of Vegetation Cover (FVC) time series from MSG to infer the ecohydrological characteristics of ecosystems over Africa. We derive a set of ecohydrological metrics from the vegetation decay period, and evaluate their spatial patterns. Our overarching hypothesis is that these metrics, derived from the vegetation dynamics over decay periods, contain valuable information on plant water access, presence of secondary moisture sources, and other ecohydrological mechanisms, which are modulated by climate, topography, soil properties, groundwater access, as well as vegetation traits and scales. The ecohydrological metrics include (i) robust estimates of the minimum and maximum FVC, (ii) FVC integral over the decay period, and (iii) the exponential decay rate during dry-down. Using the metrics, we evaluate several hypotheses that encompass the ecohydrological characteristics of moisture-limited ecosystems and the influence of environmental factors and land characteristics therein, such as:

1. In arid regions, minimum and maximum FVC are larger in sandy soil while this covariation is inverted in semi-arid and humid regions. This hypothesis follows the "inverse texture effect" (Noy-Meir, 1973) often reported in drylands.
2. Within similar climatic aridity, secondary moisture sources increase the minimum FVC and decrease seasonal FVC range. This hypothesis is derived from the classical approach of mapping groundwater-dependent ecosystems – with shallow water table or potentially larger runoff due to topography – as "green islands" of attenuated seasonality (Eamus et al., 2015).
3. Time integral of FVC over decay period as a proxy for plant accessible water storage is larger in semi-arid regions where differences between precipitation and po-

tential transpiration are marginally smaller at annual scales than at seasonal scales, compared to arid and humid regions. This hypothesis follows the expected optimal rooting depth of plants considering cost and benefit of developing root structure (Guswa, 2010).

4. FVC decay rate driven by progressive water limitation becomes lower with increasing aridity, tree cover and canopy height. This hypothesis assumes FVC mimics the decay rate of land evaporation during decay period and follows previously reported increase in timescale of land evaporation decay with aridity, canopy height, and woody vegetation (Teuling et al., 2006; Boese et al., 2019; Martínez-de la Torre et al., 2019). Therefore, FVC decay rate would reflect adaptations of ecosystem water use strategies.

We approach the analysis firstly by looking at the continental scale variations of the metrics, together with climatic aridity as the first order driver. This covariation is further scrutinised with other environmental factors relevant to the hypotheses given above. As aridity metric we chose mean annual root-zone soil moisture from the Global Land Evaporation Amsterdam Model (GLEAM).

To derive the ecohydrological metrics for the African continent from high-resolution remote sensing data (Sec. 2), we developed a robust methodology (Sec. 3) to deal with noise, gaps, widely varying dynamics, and data size. The quality diagnostics along with the derived metrics and discussion of underlying mechanisms (Sec. 4), and open code for derivations, enables future advances in understanding and modelling ecohydrological processes and variability. Furthermore, initial analysis and corroboration with independent data illustrates the potential of applications of the ecohydrological metrics (Sec. 4).

2 Data

2.1 Fraction of Vegetation Cover

The FVC, derived from a spectral mixture analysis of the satellite retrievals, is a vegetation index summarising the two-dimensional coverage ratio of vegetation per unit land area (Trigo et al., 2011). With a range of [0–1], FVC is often used to derive fundamental vegetation indices such as the Leaf Area Index. The FVC product used in this study was obtained from the Satellite Application Facility for Land Surface Analysis (LSA-SAF) of the European Organisation for the Exploitation of Meteorological Satellites (EUMETSAT). The product is based on the retrievals of the Spinning Enhanced Visible and Infrared Imager (SEVIRI) sensor on board the MSG satellite (Trigo et al., 2011). As a geostationary satellite, the MSG has a circular spatial coverage of Earth centred at 0° longitude, and it covers Europe and Africa entirely (see an example of the original FVC data for a day in Fig. A1). The SEVIRI is a multispectral optical sensor with 12 spectral bands, and a temporal resolution of 15 minutes. Under the sub-satellite point (nadir), it has 3.1 km spatial resolution in the normal bands, and a high-resolution band with 1 km spatial resolution. The spatial resolution of the retrieval decreases with distance from the nadir, as for all geostationary satellites.

The FVC data product is available at daily temporal resolution spanning the time period from early 2004 to present. FVC is estimated using parameters of a bidirectional reflectance distribution function on the cloud-corrected top of canopy reflectance values of three spectral channels namely red, near-infrared, and middle-infrared (LSA-SAF, 2016). Thanks to the very high temporal resolution of the SEVIRI sensor, spatial consistency of cloud-free data is ensured by the data providers (Trigo et al., 2011), which is also confirmed by studies comparing enhanced vegetation index products of SEVIRI and MODIS across the Congo Basin (Yan et al., 2016). Further details of the product, and access to

downloading data are available at https://landsaf.ipma.pt/en/products/vegetation/fvc/ .

For this study, we selected the spatial domain as the African continent. In order to convert the product into equal width grids to facilitate analysis with other products, we resampled the original data to spatial resolution of 0.0417° (ca. 5 km) with the nearest neighbour method (using gdalwarp function in GDAL, GDAL/OGR contributors, 2020). In terms of temporal domain, we used nearly 16 years of data, from the beginning of the records in 2004, to the end of 2019.

2.2 Ancillary Data

Soil Moisture

We used the third version of GLEAM estimates of root-zone soil moisture (Miralles et al., 2011; B. Martens et al., 2017). GLEAM consists a set of modules to estimate different components of land evaporation simultaneously. Therefore, the model estimates multiple products including root-zone soil moisture, (hereafter referred to as soil moisture). GLEAM data is available at 0.25° space and at daily resolution in time from 2003 up to date with a small latency. We used mean value of daily estimates from 2004 to 2019 (parallel to the temporal domain of FVC data used) as a diagnostic for average climatological aridity in Sec. 4. Additionally, we used daily values to compute temporal correlation between soil moisture and FVC, after aggregating original FVC data into 0.25° by simple averaging (see Appendix D for spatial variation of correlation values).

Sand Content of Soil

In order to quantify effects of soil texture, we used gridded sand percentage of soil data from SoilGrids dataset (Hengl et al., 2017), which is a machine learning based interpolation of soil profiles at 250 meter resolution. SoilGrids dataset is available globally and provides information from different layers, ranging from surface to 2 meters depth. Though in this study, for interpretability, we used the average of the top five layers that are not deeper than 1 meter for interpretability, and used the data at 0.0417° after aggregating by simple averaging.

Height Above Nearest Drainage

To relate the variation of the metrics to meso-scale heterogeneity and convergence of moisture caused by topography, we used the Height Above Nearest Drainage (HAND) data from (Yamazaki et al., 2019). Quantifying the vertical distance of a given point to the nearest drainage, HAND is closely related to drainage topology and hillslope-scale convergence of soil moisture and groundwater (Nobre et al., 2011). The HAND data used here is based on the MERIT digital elevation model at a spatial resolution of 3-arc second (ca. 90 m). We used the original high-resolution data after aggregating (simple average) to the resolution of the ecohydrological metrics presented in this study (0.0417°).

Topographic Wetness Index

In order to understand the runoff related effects of topography, we used Topographic Wetness Index (TWI), also known as compound topographic index. Being a function of both slope and the upstream area that potentially contribute to runoff of a given point, TWI is a metric to diagnose topography-induced effects on water cycle at hillslope scales. We used TWI data from Amatulli et al. (2020), which is computed by using the MERIT digital elevation model at 3-arc seconds, as the in case of HAND. In order to account for the high variability of TWI at hillslope scales while aggregating the data into 0.0417°, we first calculated median TWI value of the domain (0.069). Then, we aggregated the TWI values by calculating percentage of sub-grid cells having higher TWI values than the median value computed in the first step. Eventually, similar to TWI itself, larger val-

ues in the normalised TWI means larger potential runoff due to topographic complexity.

Accessible Water Storage Capacity and Rooting Depth

We used multiple proxies of plant accessible water to understand their effects on vegetation dynamics. Effective Rooting Depth (ERD, Yang et al., 2016) is one of those products, which is natively at 0.5° spatial resolution. ERD comes from a global parametrisation of a process-based, analytical model of carbon costs and benefits of deeper rooting in plants, proposed by Guswa (2008). In this model, the cost of deeper roots is estimated considering the physical structure of roots like density and length together with root respiration, while the benefit is estimated considering water use efficiency, growing season length and mean transpiration rate per rooting depth. In order to parametrise the model, root and soil properties were obtained from the literature, water use efficiency from an ensemble of process based models while climatological information from a long-term mean of remote sensing based products.

In addition, the Rooting Depth (RD) product from Fan et al. (2017) is also used in this study. RD is estimated with inverse modelling of root water uptake profiles in three steps, where first soil water profile, as the supply, is estimated using climate, soil properties and topography. Thanks to the availability of high-resolution information on soil and topography, RD has a much higher spatial resolution (0.0083°, ca. 1 km) than the other products. After estimation of plant water demand using atmospheric conditions and leaf area index, the supply is allocated as root water uptake using Ohm's law at different soil depths, where amount of infiltration, groundwater recharge, and subsequent uptake were effected (Fan et al., 2017). Note that the model includes multiple forcing data, with a temporal coverage from 1979 to the time of the study.

Apart from the rooting depth products, we also used estimates of plant water storage capacity. Accessible Water Storage Capacity (AWSC, S. Tian et al., 2019) is derived at 0.25° by assimilating an ecohydrological model (World-Wide Water, van Dijk et al., 2013) with different remote sensing based water observations, namely surface water extent, near-surface soil moisture and variations of terrestrial water storage. World-Wide Water is a process based model using atmospheric conditions, containing three soil layers to simulate vegetation access to soil moisture, which also accounts for recharge and discharge from groundwater. Due to the temporal availability of the forcing data, AWSC product is derived using 6 years of data starting from 2010.

The forth and last product used to analyse plant accessible water storage capacity is the Root Zone Storage capacity (RZS_{CRU2}, Wang-Erlandsson et al., 2016) product derived by contrasting water fluxes observed by remote sensing, precipitation and irrigation as influx, and evaporation as outflux. Owing the assumption that plants develop their roots to optimise their root zone storage capacity, and using a simple approach on water fluxes, Wang-Erlandsson et al. (2016) did not use any external information on vegetation or soil properties. While different precipitation data are used as forcing data with different drought return periods, we used the final product forced by Climate Research Unit precipitation data (CRU TS3.22, Harris et al., 2014) with the shortest return period, 2 year. RZS_{CRU2}, which is derived using data from 2003 to 2013, is available at 0.5° spatial resolution.

For a consistent comparison across data at different resolutions, we aggregated all data to a common spatial resolution of 0.5° by simple averaging. Note that the spatial aggregation may result in loss of the spatial variability prevalent locally and potentially captured at a high resolution. Moreover, we only used the grid cells that all products have an estimate.

Canopy Height

Since canopy height is an important indicator of ecosystem functions and is associated mostly with water limitation (Tao et al., 2016), we analysed the effects of canopy height on the decay rate of vegetation cover through their covariation in space. We used the lidar-derived canopy height data from the retrievals of the ICEsat satellite at a spatial resolution of 1 km (Simard et al., 2011). We used the data after aggregating (simple average) to 0.0417°.

Tree Cover

We used tree cover data in order to analyse the sensitivity between the relationship of decay rate of FVC and climatological aridity. We used the tree percent component of the MOD44B Version 6 Vegetation Continuous Fields from MODIS (Dimiceli et al., 2015), which is available globally in 250 meter spatial and annual temporal resolution. We aggregated the product in space to the target resolution of this study by taking the mean of higher resolution grid cells. Finally, we used the median tree cover value over the years covering the temporal domain of FVC data to obtain a time invariant metric, same approach taken for the annual estimates of the metrics derived from FVC (see Sec. 3).

3 Methodology

The derivation of the ecohydrological metrics is based exclusively on the daily FVC time series. The method can be divided into four main steps: (i) masking and retrieval of minimum and maximum FVC (FVC_{min} and FVC_{max}), (ii) detection of start and end of the decay periods, (iii) estimation of the decay period FVC integral (I_{dp}), and (iv) estimation of the FVC decay rate during dry-down (λ). Each methodological step is described in detail in the following subsections together with the final products, and their quality diagnostics when needed.

3.1 Masking and Retrieval of FVC Extrema

To remove the effect of outliers within a time series, we selected the 2nd and 98th percentiles of the entire records of the FVC data as the minimum (FVC_{min}) and the maximum asymptotic values (FVC_{max}). To maintain a reliable signal-to-noise ratio before taking further steps, we filtered out any grid cell if $FVC_{max} < 0.1$ or more than one-third of the time series were missing. Due to the simplicity of the derivation of FVC_{min} and FVC_{max} metrics, quality diagnostics were deemed unnecessary, and not derived in this set of metrics.

3.2 Detection of Decay Periods

The detection of the decay period was based on a procedure using the first derivative of the smoothed FVC (V') (see Algorithm 1). We smoothed daily time series of the FVC with a 31-day moving average (V_{sm}). Then each day in the time series was marked as decay, growth or stable. To do so, we set two thresholds for decay and growth periods as th_{decay} and th_{growth}, respectively. After rigorous investigation of time series of individual grid cells, we used the 75th and 70th percentiles of the negative derivative (V') as thresholds th_{decay} and $-th_{growth}$ for each grid cell. The magnitude th_{decay} is, thus, bigger than th_{growth}, in accordance with the larger gradient in the beginning of the period than the end. Only the magnitude of th_{growth} was taken as a positive threshold to detect the increase in FVC.

An observation was considered as decay if $V' < th_{decay}$, growth if $V' > th_{growth}$, and stable if $th_{decay} \leq V' \leq th_{growth}$. The resulting time series of classes (decay, growth, or recovery) were then smoothed by retaining the majority of decay and stable against recovery within a 5-day moving window. Complete decay period, which is considered as

the initial decay period followed by a stable, non-increasing period, was then identified as the period from the beginning of a decay to the end of a stable period. In order to ensure robustness of the end of the stable period, especially in hyper-arid regions with poor signal-to-noise ratio, we extended the detected decay periods until the next significant increase in V_{sm} ($> 5\%$ of the corresponding seasonal amplitude of FVC). Note that selection of the thresholds and the moving window sizes were based on extensive exploration and visual inspection of the FVC time series. This was a necessary step to ensure the robustness against noise in the data, as well to address the diversity of FVC dynamics across African ecosystems. To highlight the complexity, some representative time series of FVC in selected grid cells across different climatological aridity are included in Appendix B, together with soil moisture and precipitation time series.

After detection of all decay periods in the time series, we only selected the longest one per calendar year. This is necessary for regions where vegetation may potentially have two growing (and decaying) seasons within a year. The longest decay period within a year is likely to be the most indicative of the largest water limitation, and the underlying ecohydrological mechanisms. When the detected decay period spanned over two calendar years, it was assigned as the decay period of the starting year. In total, the decay period detection algorithm (Algorithm 1) yielded 16,423,339 decay periods in 1,029,847 grid cells.

Algorithm 1 Detection of decay periods from the entire time series

1: Smooth FVC time series with 31 days moving average; to yield V_{sm}
2: Calculate the first derivative of FVC time series from V_{sm} with daily step size; to yield $V^{'}$
3: Through the entire time series, set the threshold for decay as th_{decay}=percentile($V^{'}$, 75) where $V^{'} < 0$
4: Through the entire time series, set the threshold for growth as th_{growth}=-1 $\times$ percentile($V^{'}$, 70) where $V^{'} < 0$
5: Mark each observation for their corresponding period as:
    if $V' < th_{decay}$ **then** decay
    else if $V' > th_{growth}$ **then** growth
    else stable
6: Smooth the classes with a 5-day moving window by majority voting
7: Label consecutive observations marked with decay and followed by stable ones as *decay period*
8: Extend every *decay period* label until $V_{sm} > min(V_{sm}) + 0.05 \times (max(V_{sm}) - min(V_{sm}))$ is satisfied in the corresponding season
9: For each grid cell, keep only the longest *decay period* per year

3.3 Estimation of the Integral over FVC Decay

We calculated the integral of FVC during decay period (I_{dp}) as the total area under the FVC time series from the start to end of the decay period, with the area under FVC_{min} removed. This can be expressed as,

$$I_{dp} = \sum^{decayperiod} (FVC(t) - FVC_{min}) \tag{1}$$

Removal of the baseline FVC value (FVC_{min}) enhances the signal of seasonal decay of vegetation with respect to baseline vegetation activity. Note that, upon necessity, the full integral (total area under the curve) can be calculated as the sum of I_{dp} and multiplication of decay period duration with minimum FVC ($D \times FVC_{min}$).

From the yearly dry season detection, 16 (the number of years) values of I_{dp} were computed for each grid cell. We selected the median of the 16 values as the representative inference to be used for spatial analyses. The median was preferred over the mean to make the estimation robust against annual variations, for instance, by intermittent rain events in the dry season or issues related to FVC derivation. In addition, we also calculate and report the normalised robust Standard Error (SE) as an indicator of variability. The SE is calculated as,

$$SE = \frac{SD_n}{\sqrt{n}} \tag{2}$$

where SD_n is the robust standard error, calculated from the Median Absolute Deviation (MAD) across years (with the assumption of a normal distribution, Rousseeuw & Croux, 1993), and corrected for the low number of samples ($n = 16$) as:

$$SD_n = MAD \times 1.4826 \times \frac{n}{n-1} \tag{3}$$

The robust standard error reflects variability of the metrics among years as well as methodological uncertainty, and is therefore suitable for customised filtering in the context of spatial analysis.

3.4 Estimation of FVC Decay Rate

Temporal decay of the FVC can be characterised using an exponential function as,

$$FVC(t) = (FVC_{dd} - FVC_{min}) \times e^{-t/\lambda} + FVC_{min} \tag{4}$$

where FVC_{dd} is the initial FVC value in the beginning of a dry-down, and λ is the e-folding time (in days). Note that λ is merely an inverse of the exponential decay rate. The formulation in Eq. 4 uses λ as it is easier to interpret. In simple terms, λ denotes the number of days needed to have a decrease in the seasonal amplitude of FVC ($FVC_{dd} - FVC_{min}$) to $1/e$ of its original value during a dry-down event. Note that the selected exponential decay function explicitly takes an asymptotic minimum value of the FVC, as FVC_{min}, into account while estimating the decay rate (see Sec. 3.1) since FVC_{min} is included in the formulation (Eq. 4).

Due to the S-shaped character of temporal vegetation dynamics, functions allowing different convexity, e.g., logistic functions, have been used to characterise these dynamics (Beck et al., 2006). As exponential decay functions are strictly convex, the concave part of the decay, which is mostly observed in the beginning of the decay period, is not considered for this metric. The latter part of the decay period, with convex curvature (i.e.: the first derivative is negative while the second is positive), is labelled as 'dry-down' during the decay period. To define the dry-down period, we first discarded the time steps with concave observations (negative first and negative second derivative). Afterwards, we filtered out the convex observations before the inflection point of the FVC, that mostly associated with low signal-to-noise ratio at the beginning of the dry-down. Once daily observations are marked as convex or concave, we searched for local minimum of V' in the first third of the dry season, and identified the inflection point as the start of the dry-down. Note that, in the above process, second derivative of the FVC (V'') was also smoothed with a 31-day moving window.

This procedure effectively removes observations with concave shape in the dry season, especially at the beginning of an event. For each event, if more than half of the data points showed convexity, we estimated λ, together with FVC_{dd}, based on an asymptotic

Algorithm 2 Identification of dry-down periods and modelling of the exponential decay

1: Smooth $V^{'}$ with 31 days moving average; to yield $V^{'}_{sm}$
2: Calculate the second derivative of FVC time series from $V^{'}_{sm}$ with daily step size; to yield $V^{''}$
3: Smooth $V^{''}$ with 31 days moving average; to yield $V^{''}_{sm}$
4: Mark each observation with $V^{'}_{sm} < 0$ as:
    if $V^{''}_{sm} > 0$ **then** convex
    else concave
5: Ignore convex observations before the inflection point of FVC time series, if there is any
6: Ignore concave observations within the decay period and keep the rest as the dry-down period
7: Discard any event having more concave observations than convex
8: Use Eq. 4 on dry-down period of the decay period to estimate λ
9: Filter out the estimations with $NSE < 0.5$ OR $SE(\lambda) > 0.5 \times \lambda$

regression model that minimises least squares error with the Levenberg–Marquardt algorithm (Moré, 1978; Elzhov et al., 2016). We used both the Nash–Sutcliffe modelling efficiency (NSE; Nash & Sutcliffe, 1970) and the standard error of the model (SE_m) to assess the estimates of the model fitting. From the multiple λ estimates, only those with successful convergence of the Levenberg–Marquardt algorithm with NSE > 0.5 and $SE_m(\lambda) < 0.5 \times \lambda$ were accepted, the median of which was taken as the representative final λ for a grid cell.

After defining the final λ, we estimated the variation as done in Sec. 3.3. Unlike in Sec. 3.3, the sample size per grid cell (n) may change, as λ estimation may not converge in cases with high noise. We, therefore, also report the number of successful convergences of the Algorithm 2 as an additional quality diagnostic that can be used for filtering λ (mapped in Fig. H1).

4 Results and Discussion

In this section, we present and discuss the ecohydrological metrics derived in this study. For each metric we show the spatial variation in continental scale by maps along with zoomed inset plots (see Appendix E for further information and visual impression by corresponding Google Earth cut-outs) to visualise regional variability. Box plots of metrics per mean annual root-zone soil moisture show first order variations while heatmaps show sensitivity of these first order variations to different parameters addressing the hypotheses given in Sec. 1 (see Sec. 2.2 for the details of the data). Here we present the metrics independently, but we summarise their cross-comparison with a density plot in Fig. C1.

4.1 FVC Extremes

Spatial distributions of FVC_{min} and FVC_{max}, histograms of the distribution over the full domain, and six zoomed insets focusing on selected regions are shown in Fig. 2a and 2b, respectively (see Fig. F1 for the seasonal dynamics expressed as $FVC_{max}-FVC_{min}$). At the continental scale, both FVC_{min} and FVC_{max} follow the moisture gradient with the highest and the lowest values in humid and arid regions, respectively. Saturation in the increase of FVC_{max} (Fig. 2c) in semi-arid regions suggests that water does not severely limit the vegetation cover at the peak of the wet season in regions with intermediate to high mean annual soil moisture values (see Fig. E1 for map of mean annual root-zone soil moisture as an indicator of climatological aridity together with Google Earth views

of the insets). On the contrary, FVC_{min} stays low up to intermediate mean annual soil moisture and increases only slightly with it suggesting that water limits FVC severely at the peak of the dry season. Understandably, largest seasonal ranges in FVC are observed in regions with semi-arid climate systems.

In addition to the climate-associated large-scale gradients, the metrics also exhibit a substantial meso-scale heterogeneity. In arid regions, FVC_{min} is higher in areas closer to perennial water sources, as can be seen near the Senegal and Gambia rivers (Box-A in Fig. 2a). FVC_{min} is also elevated near large inland deltas and wetlands, i.e. the Okavango Delta (McCarthy, 2006) and the Sudd swamp (Tootchi et al., 2019), Box-D and Box-F in Fig. 2a, respectively, presumably indicating groundwater access by the vegetation in the dry season. Interestingly, the meso-scale spatial patterns differ remarkably between FVC_{min} and FVC_{max} with a tendency of FVC_{max} showing more spatial structure than FVC_{min}. This is likely because there is too little water input in the dry season to cause big topographic moisture effects for FVC_{min} except for the perennial secondary water sources. Thus, such meso-scale heterogeneity suggests the importance of secondary water sources in water-limited systems, especially on top of the large climate-driven spatial variations, and highlights the value of FVC_{min} and FVC_{max} for ecohydrological studies.

Inverse Texture Effect

We further tested if an "inverse texture effect" (Noy-Meir, 1973) could be observed from 5 km spatial resolution remote sensing FVC data over continental Africa. In humid regions coarse textured soil is less favourable for vegetation than fine textured soil while in arid regions this pattern is inverted. This inverse texture effect has been documented by several site-scale studies (Sala et al., 1988; Laio et al., 2001; Fernandez-Illescas et al., 2001; Looney et al., 2012). Noy-Meir (1973) suggested this inversion to occur with precipitation values of 300–500 mm/year, although it has also been reported for higher precipitation values (Epstein et al., 1997). The inversion of the texture effect in arid climates is likely due to enhanced infiltration and hydraulic conductivity which reduced soil evaporation losses (Noy-Meir, 1973) and/or due to reduced water stress thanks to lower matrix potentials of sandy soils (Caylor et al., 2005).

We binned soil moisture and sand percentage values to have equal number of observations in each bin of a given variable, and calculated the mean of FVC_{min} or FVC_{max} per bin. The resulting heatmaps in Fig. 3 do not show clear patterns of an inverse texture effect where FVC would be expected to increase with sand content. In the driest regions with the lowest mean annual soil moisture level, FVC_{min} and FVC_{max} are slightly elevated for low sand content, consistent with the "normal" texture effect. For intermediate aridity levels, no clear and systematic pattern with sand content can be observed. It remains for further studies to clarify to what extent the "inverse texture effect" remains significant, which may be due to spatial resolution and quality of remote sensing data.

Green Islands

Another phenomenon we investigated are the "green islands" patterns where localised moisture availability supports vegetation activity in otherwise dried down conditions. This approach has been used to detect groundwater dependent ecosystems (Münch & Conrad, 2007; Howard & Merrifield, 2010; Jin et al., 2011; Lv et al., 2013; Barron et al., 2014) or riparian corridors (Everitt & Deloach, 1990; Everitt et al., 1996; Neale, 1997; Akasheh et al., 2008) based on high spatial resolution remote sensing within relatively small regions. Here we analyse if such patterns due to secondary moisture sources are still evident at 5 km resolution and at continental scale by looking at the covariation of FVC_{min} and FVC_{max} with HAND and TWI, conditioned on mean aridity (Fig. 3). HAND is a hillslope scale proxy for groundwater accessibility (Fan et al., 2019) while TWI, a

metric considering local slope together with upstream area, is a strong proxy for topographic soil moisture variations (Raduła et al., 2018). Contrary to our expectations, we did not observe a positive effect of these secondary moisture resources in arid regions on FVC_{min} (Fig. 3a) but instead for FVC_{max} at high aridity levels (Fig. 3b). This implies that shallow water table support vegetation with additional moisture during the growing period as also shown in Koirala et al. (2017) but that this effect largely disappears in the dry season since most of the secondary moisture resource is also depleted or not available. This suggests that the effect of secondary moisture sources goes much beyond the frequently studied perennial "green islands" phenomenon and is likely more important in the wet rather than the dry season.

4.2 Integral of FVC Decay

Integral of FVC time series during decay period, I_{dp}, is smallest in arid regions, followed by humid regions while the largest I_{dp} values are observed in semi-arid regions (Fig. 4a). Median values, as well as variations of I_{dp} within similar climatology is larger when subject to intermediate aridity (Fig. 4c). Uncertainties are larger in some of the hyper-arid regions with low FVC and rare, episodic rainfall (Fig. 4b).

At local scales, variations in I_{dp} emerge as a combined effect of climate and other ecohydrological factors change over hillslope scales, such as proximity to the nearest drainage or occurrences of shallow water table depth. While a sharp aridity gradient in Sahel is clearly seen at Box-A and Box-B of Fig. 4a, local scale increases in I_{dp} are also present at riparian zones like Senegal River (Box-A in Fig. 4a). Within similar aridity, I_{dp} is smaller in seasonally flooding regions like the Sudd swamp (Tootchi et al., 2019), Box-F in Fig. 2a. The highest values of I_{dp} in the Lower Zambezi, bear strong similarity with the rooting depth product presented in Wang-Erlandsson et al. (2016), and the previously reported seasonal hydrologic buffer (Kuppel et al., 2017) in these regions. This motivates further analysis of I_{dp} with a plant accessible water storage perspective.

Plant Accessible Water Storage

Conceptually, plant accessible water storage is related to the vertical distribution of roots, and the water holding capacity of the soil that is determined largely by texture and organic carbon content. The root profile of water-limited ecosystems appears to adapt to the prevailing hydrologic and soil conditions while being constrained by other ecosystem properties and traits (Guswa, 2008; van Wijk, 2011; Fan et al., 2017; Schenk, 2008; Schenk & Jackson, 2002; Laio et al., 2006). Plant accessible water storage controls the propensity and sensitivity of ecosystems to drought stress in dry periods. Various modelling approaches to infer rooting depth or plant water storage capacity have been proposed (explained in detail in Wang-Erlandsson et al., 2016), as it cannot be observed directly but still contains a critical information for global-scale models (Kleidon & Heimann, 1998).

The integral of FVC during dry season should be positively correlated with plant accessible water storage of the soil, as larger water storage would facilitate vegetation activity for longer period during water-limited conditions. The continental-scale patterns of I_{dp} (Fig. 4a) with the largest values in strongly seasonal semi-arid savanna systems of both hemispheres are qualitatively consistent with the previous observation-based analysis (e.g. Schenk & Jackson, 2002) as well as the optimality-based models (e.g. Kleidon & Heimann, 1998). I_{dp} declines in hyper-arid regions like the Sahel, Horn of Africa, Southern Africa, as well as the Congo rainforest. A similar pattern would be expected for optimal rooting depth, which increases in regions with small differences between rainfall and potential evaporation in annual scales but large differences in seasonal scales (Laio et al., 2006; van Wijk, 2011). The inset plots in Fig. 4a clearly reveal the landscape scale patterns of I_{dp}, presumably, due to topography-driven large variations of moisture. This may reflect enhanced and continued moisture supply due to topographic moisture con-

vergence or shallow water tables along with possible adaptations of rooting depth to these local hydrological conditions (Fan et al., 2017).

We compared I_{dp} with 4 products related to plant accessible water storage, namely two storage capacity products from Wang-Erlandsson et al. (2016) and S. Tian et al. (2019), and two rooting depth products from Yang et al. (2016) and Fan et al. (2017) at 0.5° across Africa (see Sec. 2.2 for product details). As shown in Fig. I1, there is qualitative agreement of large values of I_{dp} with $AWSC$ and RZS_{CRU2} in the Miombo woodlands and, to a lesser extent, also in the northern savannas. All three also agree on low values in hyper-arid regions like the Sahel, Horn of Africa and in Southern Africa. In order to quantify the extent of agreement among the five estimates, we made a pairwise comparison of Spearman's correlation coefficient per climatological aridity via soil moisture (Fig. 6a). While the overall low-to-moderate correlation values among the products available in the literature demonstrate the scale of the challenge in estimating plant water storage capacity or rooting depth, highest correlation was observed between I_{dp} and RZS_{CRU2}. Regardless of the product pairs, correlations decrease with increasing humidity, which is presumably related with other limiting factors than water, such as radiation or nutrients.

All four independent products utilised meteorological input data for water balance estimation, and also use remotely-sensed vegetation products in some way. While RZS_{CRU2} and $AWSC$ are constrained by hydrological Earth observations, the rooting depth products RD and ERD originate largely from different assumptions of optimality and plant adaptation. Our comparison suggests that estimating plant accessible water storage based on Earth observation data may be more suitable than the presently-used optimality principles over the given resolution and domain of this study, despite the uncertainties of remote sensing data. Using I_{dp} as an indicator of plant accessible water storage has the advantage that it is derived from dense time series of a geostationary satellite alone, requiring no additional meteorological inputs or modelling assumptions that introduce their inherent uncertainties. Furthermore, I_{dp} features higher spatial resolution than most other storage capacity data, which provides insights on subsurface moisture variations at meso-scales.

4.3 Decay Rate of FVC

Similar to I_{dp}, the e-folding time (λ), presented in Fig. 5a, also has a hump-shaped covariation with climatological aridity at continental scales. We find the lowest λ values throughout the humid regions and partially in the arid regions, such as edges of the Sahara desert or the Horn of Africa, while the highest λ values are found in the semi-arid and arid regions. Though variation of λ (Fig. 5b) suggests that the low values of λ in some hyper-arid regions are associated with higher uncertainty due to low signal-to-noise ratio.

Besides the coherent continental-scale spatial patterns, λ also has strong variations over meso-scales. Stronger lateral moisture convergence positively affects the λ in the arid regions, as seen in the Senegal (Box-A, Fig. 5a) and the Niger (partially in Box-B, Fig. 5a) rivers' riparian zones in the arid climate. However, lateral moisture convergence does not always affect λ positively, as seen in the riparian zones of the Upper Zambezi and the Okavango rivers and their tributaries. Shown in Box-D in Fig. 5a, λ is high around the Cuando river, the Okavango Delta and the Linyanti swamp, but low in the Barotse Floodplain (see Cronberg et al. (1995); Zimba et al. (2018) for general information about the region). Such non-trivial patterns suggest the role of complex interactions between the vegetation traits and local moisture conditions (Fan et al., 2019), which also affect λ.

λ and Ecosystem Water Use

λ can corroborate the rate of decrease of plant available water, ecosystem scale water use efficiency, and the propensity to senescence. Ecosystems differ widely in their water use strategies, from being water conservative – typically associated with strong down-regulation of stomatal conductance with water deficiency – to aggressive exploitation of water resources (Laio et al., 2001). Herbaceous plants are typically aggressive water users and cease with the depletion of surface soil moisture. Woody plants risk cavitation and death under severe water stress, and such, trees in places with frequent dry periods benefit from a water saving strategy or senescence for prolonged periods. Konings and Gentine (2017) inferred ecosystem water-use strategies globally based on diurnal variations of vegetation optical depth assuming that those reflect stomatal regulation to maintain leaf-water potential. They found an increase in isohydricity, i.e. the degree of stomatal regulation and subsequent water savings, with increase in vegetation height, consistent with the need of tall trees to prevent hydraulic failure during drought. Teuling et al. (2006) characterised decay rate in land evaporation (soil evaporation and transpiration) under water limitation using flux tower measurements and found that sites with stronger seasonality and larger woody coverage have slower decays. This association is confirmed by similar studies, for seasonality and canopy height (Boese et al., 2019), and for trees than grasses (Martínez-de la Torre et al., 2019). Slower decay of land evaporation of taller/woody canopy despite the faster decay of soil moisture with stronger aridity (McColl et al., 2017) suggests reduced transpiration or other plant adaptation mechanisms.

If the rate of FVC decay was also related to ecosystems' water use strategy in a similar manner, we would expect slower FVC decay (higher λ) with increasing canopy height. In arid and semi-arid regions, we indeed find a tendency of increasing λ with canopy height except very tall canopy (Fig. 6b), suggesting that λ incorporates ecosystem water use strategy traits as well as direct or indirect effects of soil moisture therein. However, as the climate gets wetter λ tends to decrease with canopy height. A possible explanation would be the changes in the drought coping strategies in ecosystem scale (Singh et al., 2020), or that water consumption, i.e. transpiration, increases with canopy height resulting in a faster depletion of moisture storage (Koirala et al., 2017), or increasing ecosystem water use efficiency with aridity.

Sensitivity of the nonlinear relationship between λ and climatological aridity to tree cover (see Fig. 6b) shows that λ systematically increases with larger tree cover values in arid and semi-arid systems, with peak values observed in semi-arid regions with $26-43\%$ of tree cover which overlaps with the reported interval for the transition between highly water-stressed forest and savanna (Singh et al., 2020). However this trend is inverted moving towards regions with weaker water-stress, hence denser tree cover, which agrees with Singh et al. (2020) as moderately or lowly water-stressed forests do not develop strong adaptation against water limitation, nor change canopy structure. The agreement among these two studies having different methodologies shows the value of the observation-driven metric λ to gain ecohydrological insights and have a better understand in vegetation–water dynamics.

5 Conclusions

Using retrievals of the SEVIRI sensor of the geostationary satellite MSG, we derived ecohydrological metrics for continental Africa entirely from the temporal dynamics of the daily Fraction of Vegetation Cover (FVC) time series from 2004 to 2019 at ca. 5 km ($0.0417°$) spatial resolution. Our metrics captures both continental scale gradients and covariations with climate as well as structured regional variations, e.g. due to topographic factors. This provides an unprecedented opportunity to improve our understanding of ecohydrological processes across spatial scales over Africa.

The minimum asymptotic value of vegetation cover (FVC_{min}) can be used to diagnose riparian corridors, seasonal wetlands and floodplains in arid and semi-arid regions

with its structured spatial variations over meso-scales. The maximum asymptote of FVC (FVC_{max}) shows enhanced vegetation growth in arid and semi-arid regions where ecosystem benefits from shallow groundwater or larger runoff. Therefore, FVC_{max} may be used to diagnose the effect of secondary water resources in semi-arid regions in meso-scales. At continental scales, FVC_{min} did not show a clear pattern neither for "inverse texture effect" nor "green islands", which motivates further studies to understand the extent of such local scale processes over large domains, using remote sensing. However, we observed positive effect of proximity to groundwater and runoff potential on FVC_{max} on arid regions as "green islands", which suggests FVC_{max} can reveal importance of secondary water resources in growing seasons in arid regions.

The integral of FVC time series in decay period (I_{dp}) can be used to diagnose the buffering capacity of vegetation on moisture limitation and shows broad consistency with inferred variations of the plant storage capacity or rooting depth. Since plant accessible water storage is an important, also an uncertain, aspect in ecohydrology, I_{dp} may help understand and model ecohydrological processes more accurately. The spatial patterns of I_{dp} may be used to analyse plant water storage capacity in ecohydrological models and improve simplistic approaches where this varies only with vegetation type and soil.

The last metric presented in this study, the e-folding time of vegetation cover during dry-down (λ), reveals the seasonal decay rate of vegetation, which – in the case of water-limited regions – emerges from the complex ecohydrological interactions between moisture availability and vegetation. Both the continental scale patterns against aridity and its sensitivity to canopy height and tree cover of λ agrees with the plant adaptation strategies proposed in the literature. This provides a consistent diagnostic power on vegetation water interactions over the African continent. Moreover, strong and structured variations of λ at meso-scales motivate in-depth analyses of the metric to resolve ecohydrological interactions at finer scales, yet over a continental gradient.

Overall, given the the large amount of information stored in spatial variations of the metrics reflecting different driving mechanisms across spatial scales, the metrics have great potential to improve our understanding on vegetation dynamics on: (i) testing hypotheses on understanding relevance of local-scale ecohydrological processes over large domains like continental Africa, (ii) better understanding basic ecosystem properties like water usage in ecosystem scale and diagnosing their driving factors, and (iii) extracting information and reducing uncertainty on concepts like plant water storage capacity. There remain multiple opportunities for further synergistic exploitation with retrievals of surface temperature from geostationary satellites which could provide complementary indicators on variations of moisture states inferred from an energy balance perspective. The suggested algorithms for deriving the metrics and the provision of the code facilitates consistent parallel assessments and helps overcome the technical difficulties of dealing with large volumes of data and the particularities of vegetation cover retrievals from the geostationary satellites.

6 Data and Code Availability Statement

All ecohydrological metrics presented in this study are available in standardised netCDF data format in `https://doi.org/10.6084/m9.figshare.14987211.v1`, together with their quality diagnostics.

The R scripts developed for the implementation of the methodology are available for research uses. They can be accessed through `https://github.com/caglarkucuk/EcohydroMetrics_Africa.git`.

All the data used in this study are available in the cited literature (see Sec. 2), except the AWSC data from S. Tian et al. (2019) which was obtained from the corresponding author.

Acknowledgments

Çağlar Küçük acknowledges funding from the International Max Planck Research School for Global Biogeochemical Cycles. Diego G. Miralles acknowledges funding from the European Research Council (ERC) under grant agreement 715254 (DRY2DRY) and the European Union Horizon 2020 Programme project 869550 (DOWN2EARTH).

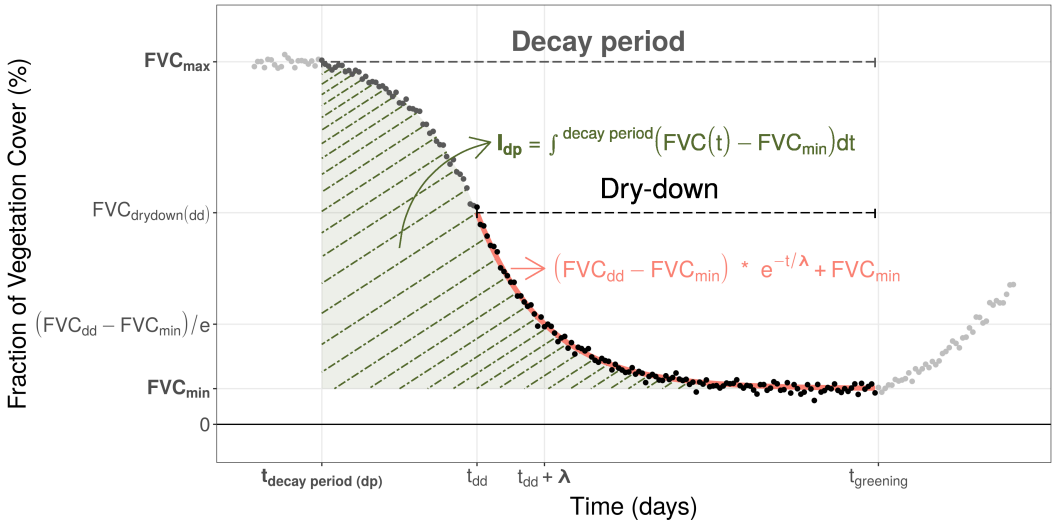

Figure 1: Conceptual plot of the ecohydrological metrics derived from time series using synthetic data. Points represent observations for growing period, early decay period and decay period with dry-down in light grey, grey and black, respectively. Decay and growth periods are defined by presence of decay, i.e., first derivative of the time series, while dry-down period is defined by the convexity of the decay, i.e., using both first and second derivatives (see Sec. 3.4 for details). The shaded area shows the integral of FVC during decay period. The red curve shows the fitted line on the FVC time series during dry-down using the asymptotic exponential decay function. All metrics presented in this study are shown in bold characters.

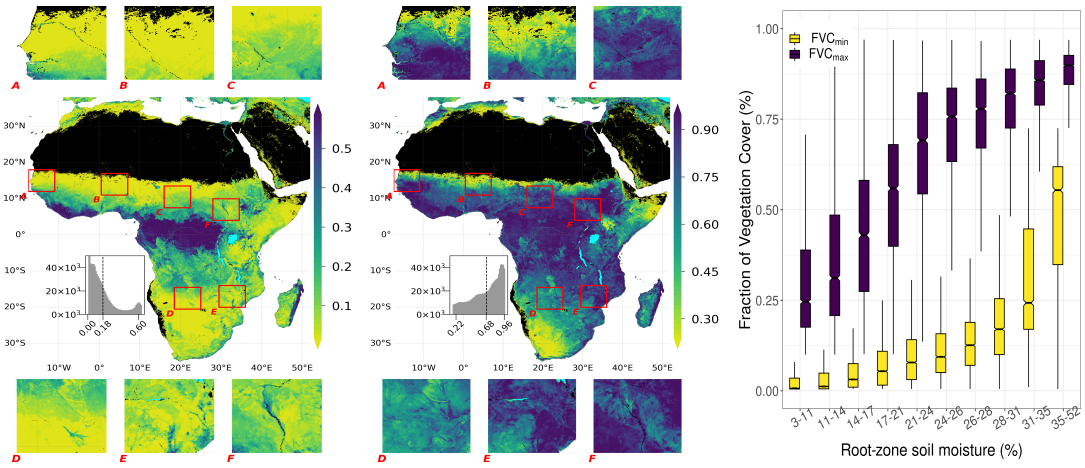

(a) (b) (c)

Figure 2: (a) Minimum asymptotic values of FVC, FVC_{min}, (b) maximum asymptotic values of FVC, FVC_{max}, (c) box plot showing the variation of FVC_{min} and FVC_{max} with mean annual soil moisture. In the maps, histogram of the metrics mapped can be seen inside the main panel, with a dashed line indicating the mean values of the domain, as well as six insets to show local variability (See Appendix E for details of the insets). In all of the following box plots, binning of soil moisture is done automatically to equalise frequency of observations among the bins while median values per each bin are shown in the intermediate line of the boxes, with their 95 % confidence intervals notched. Upper and lower edges of the boxes show the interquartile range (75th and 25th percentiles, respectively) while the error bars show 1.5 times the interquartile range.

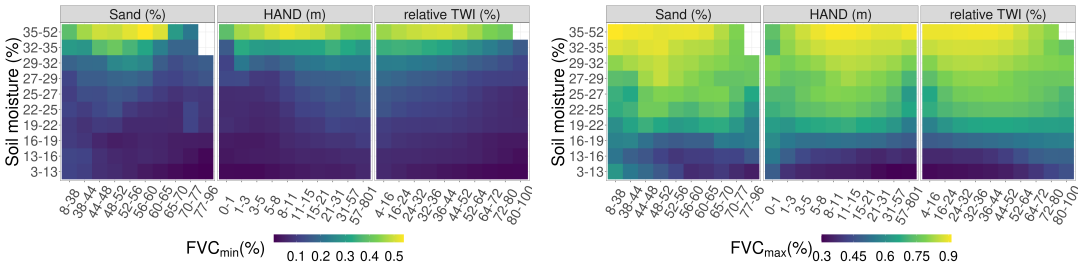

(a) FVC_{min} (b) FVC_{max}

Figure 3: Covariation of asymptote-related metrics and root-zone soil moisture with sand percentage, HAND, and TWI. Note that binning of the continuous variables in x- and y-axes are done automatically to equalise frequency of observations among the bins of a given variable.

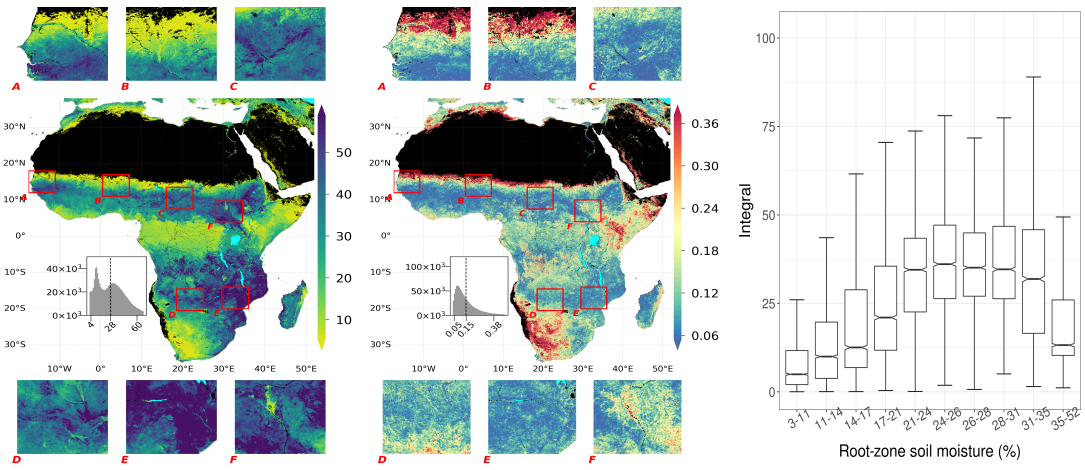

(a) (b) (c)

Figure 4: (a) Integral of FVC time series in the decay period, I_{dp}, (b) variation of I_{dp}, (c) distribution of I_{dp} within mean annual soil moisture. See Fig. 2 for plotting details.

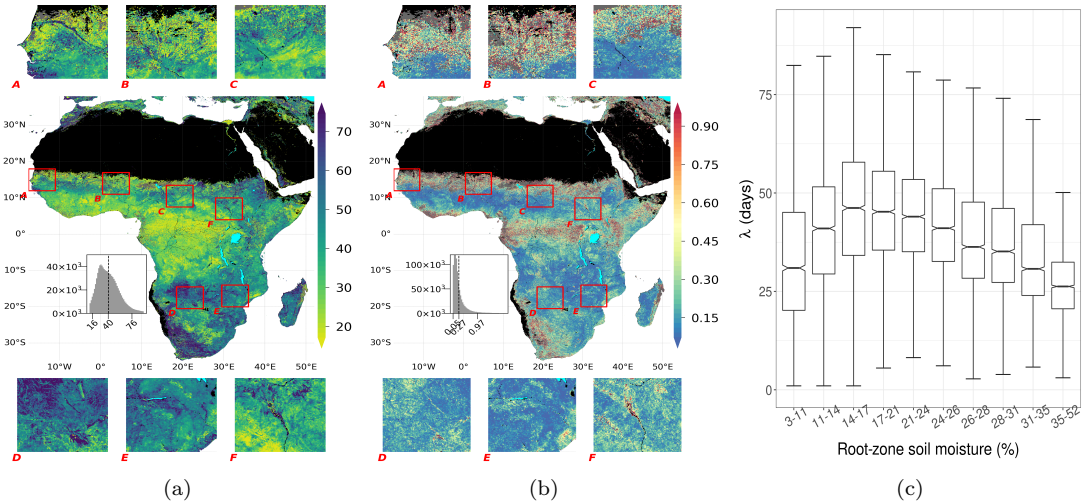

(a) (b) (c)

Figure 5: (a) e-folding time of FVC time series during dry-down (in days), λ, (b) variation of λ, (c) distribution of λ within soil moisture. See Fig. 2 for plotting details.

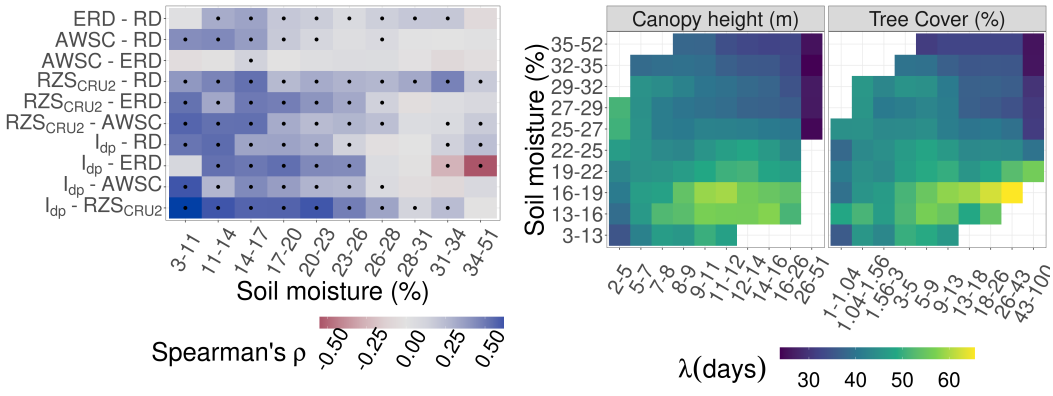

(a) (b)

Figure 6: (a) Spearman's correlation coefficients between pairs of products related to plant accessible water content, namely Effective Rooting Depth (ERD) from Yang et al. (2016), Rooting Depth (RD) from Fan et al. (2017), Accessible Water Storage Capacity (AWSC) from S. Tian et al. (2019), Root Zone Storage Capacity (RZS_{CRU2}) from Wang-Erlandsson et al. (2016), and integral of FVC during decay period (I_{dp}) presented in this study. Black dots indicate significant correlation with $\rho > 0.05$. (b) Covariation of λ and root-zone soil moisture with canopy height, and tree cover. Note that binning of soil moisture, canopy height and tree cover are done automatically to equalise frequency of observations among the bins of the given variable.

Appendix A An Example Map of the Original FVC Data for a Single Day

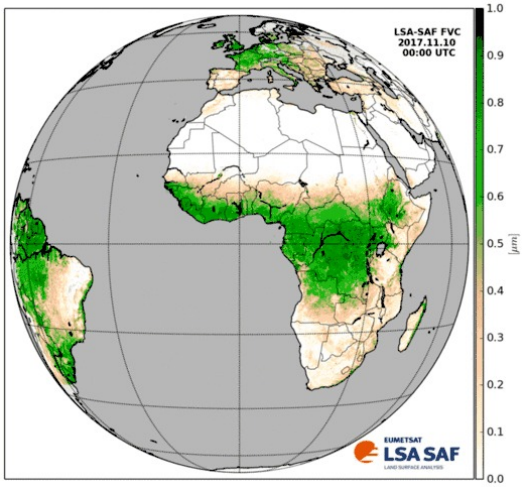

Figure A1: The original FVC data product for a single day, taken from https://landsaf.ipma.pt/en/products/vegetation/fvc/

Appendix B Time Series of FVC in Example Grid Cells

In this subsection; we present 5 years time series of selected grid cells from each bin of mean annual soil moisture values given in the main manuscript to demonstrate the results of the algorithms in grid cell scale.

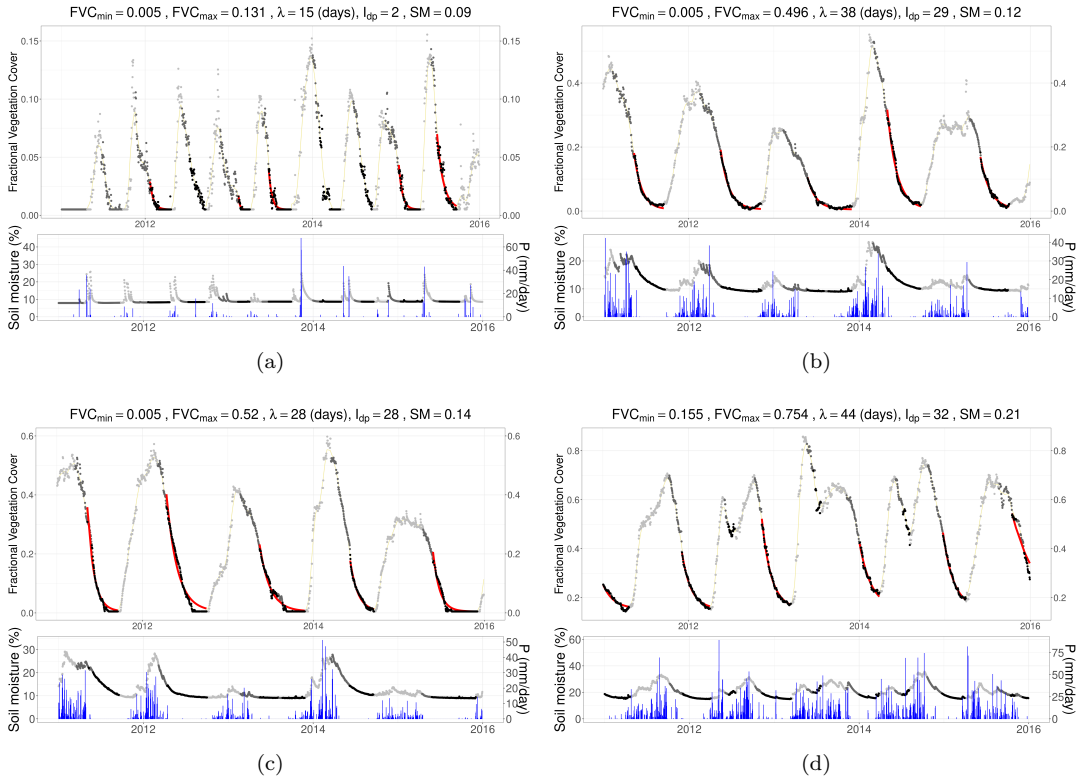

Figure B1: FVC, soil moisture, and precipitation time series of sampled grid cells. Sampling is done to have one grid cell per each bin of soil moisture values given in the plots of the main manuscript. Points for both FVC and soil moisture are coloured according to the state of vegetation activity as growing period is shown in light grey, decay period with dark grey while dry-down during the decay period is shown in black. Fitted curve to estimate λ is shown with red lines while 31-day smoothed FVC values are shown in orange lines at the upper panel, while daily precipitation values are shown with blue bars at the lower panel. Note that daily aggregated precipitation data is obtained from Tropical Rainfall Measuring Mission (TRMM) (2011).

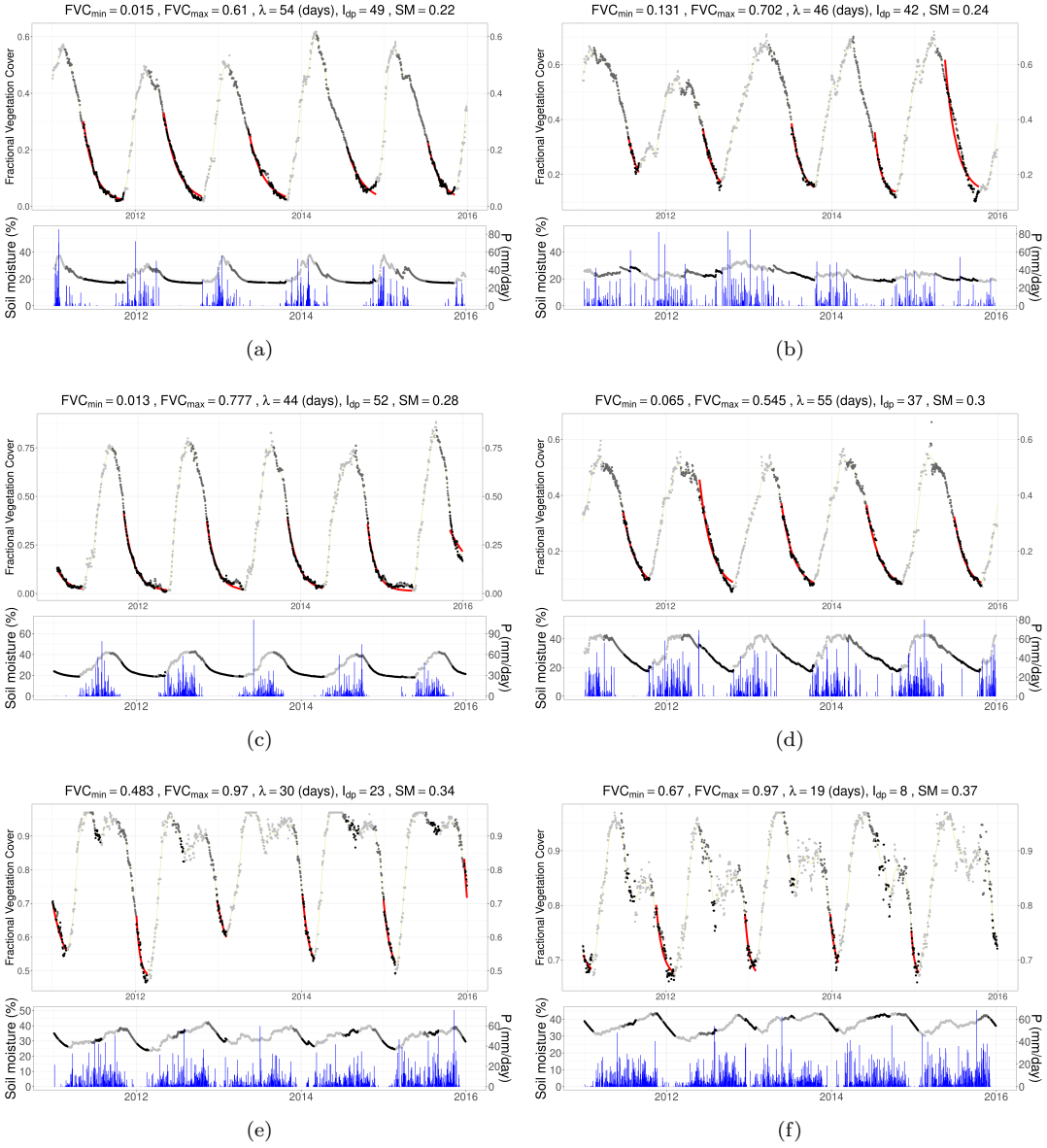

Figure B2: Continuation of Fig. B1 with samples having larger mean annual soil moisture.

728 # Appendix C Density Plots of the Ecohydrological Metrics

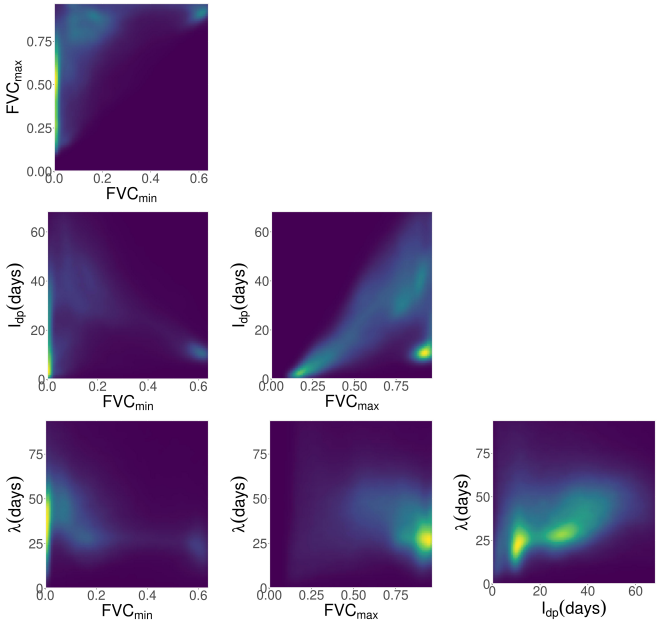

Figure C1: Density plots of the ecohydrological metrics presented in this study.

729 # Appendix D Temporal Correlation Between FVC and Soil Moisture

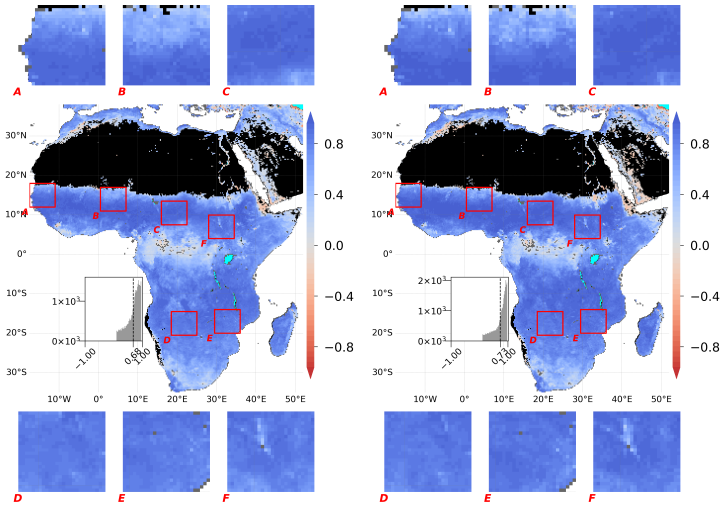

Figure D1: Pixelwise Spearman's correlation of FVC and GLEAM root-zone soil moisture in time for (a) entire time series, (b) time series marked as decay period using FVC.

Appendix E Map of Climatological Aridity and Google Earth View of Insets

Fig. E1 shows the continental map of mean annual root-zone soil moisture (%) from GLEAM and the Google Earth views of the insets. Note that soil moisture values are binned to have equal number of observations in each class. Box-A: the Gambia and large portion of the Senegal rivers; Box-B: a small area of the Niger river mostly showing the transition from the Sahara desert to Sahel; Box-C: more on the transition from Sahel to tropical regions; Box-D: located in one of the most complex regions of Africa in terms of topography and lateral flow of water with lower sections of the Okavango and the Cuando rivers and upper section of the Zambezi river, together with multiple seasonally flooding areas like the Okavango delta, the Barotse Floodplain, and the Linyanti swamp. These seasonal wetlands are vital for the ecosystem and also provides great support against water limitation and heat for not only plants but also animals; Box-E: Lower Zambezi Basin together with the drainage of Lake Malawi to Zambezi. It also covers the Inyanga mountains located between Mozambique and Zimbabwe where a climatic shift happens over the mountain range. Last but not least, Box-F: largely covered by tropical savanna, is divided by the White Nile from South to North, covers the Sudd swamp.

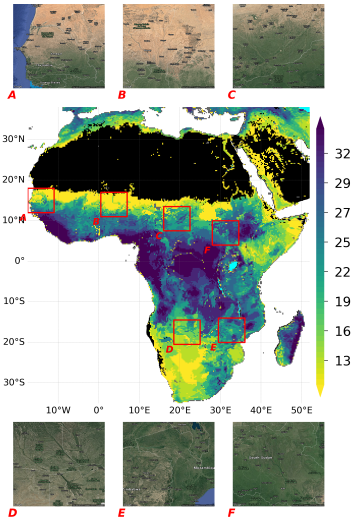

Figure E1: Map of mean annual root-zone soil moisture (%) in the centre and satellite view of the insets. Map and image data of the insets: Google Earth ©2020 TerraMetrics.

747 # Appendix F Summary of Seasonal Dynamics of FVC, FVC_{range}

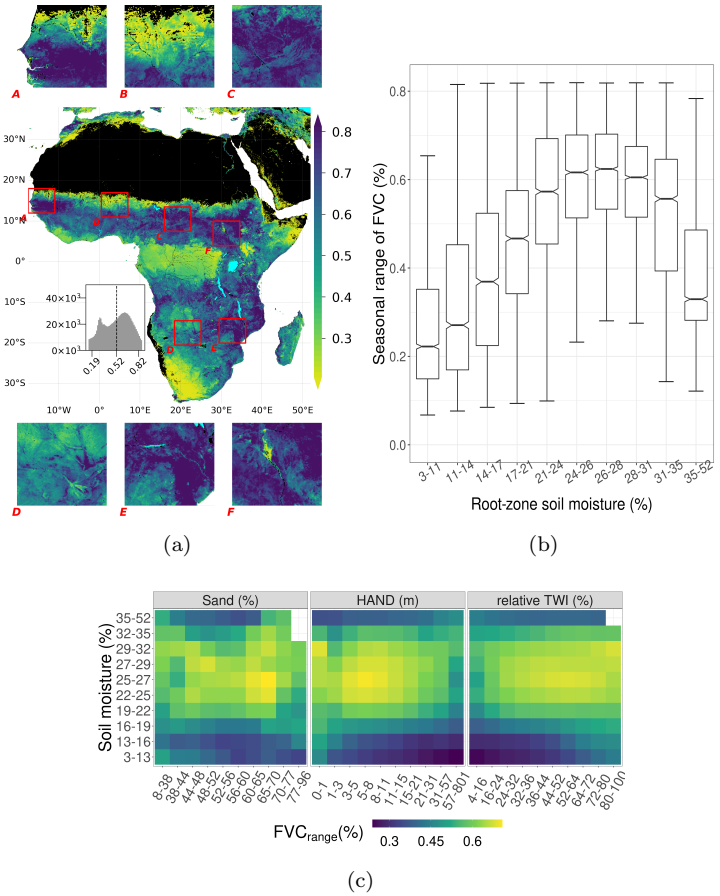

(a) (b)

(c)

Figure F1: Variations in FVC_{range} (as $FVC_{max} - FVC_{min}$) (a) in space (b) with climatological aridity (c) similar to Fig. 3a but for FVC_{range}

Appendix G Map of I_{dp} Normalised by Event Duration

In order to see the effect of event duration to I_{dp}, we normalised the I_{dp} values with the duration of the specific event I_{dp} is estimated. Even though spatial patterns remained largely the same after normalisation, they became more pronounced in the East Sudanian Savanna and Miombo woodlands in the Southern Africa. Spatial distribution of the normalised I_{dp} is mapped, together with its covariation with soil moisture and the original I_{dp} is shown in Fig. G1. Note that duration of the event necessary to make the normalisation is available in the corresponding netCDF file of the metrics (see Sec. 6).

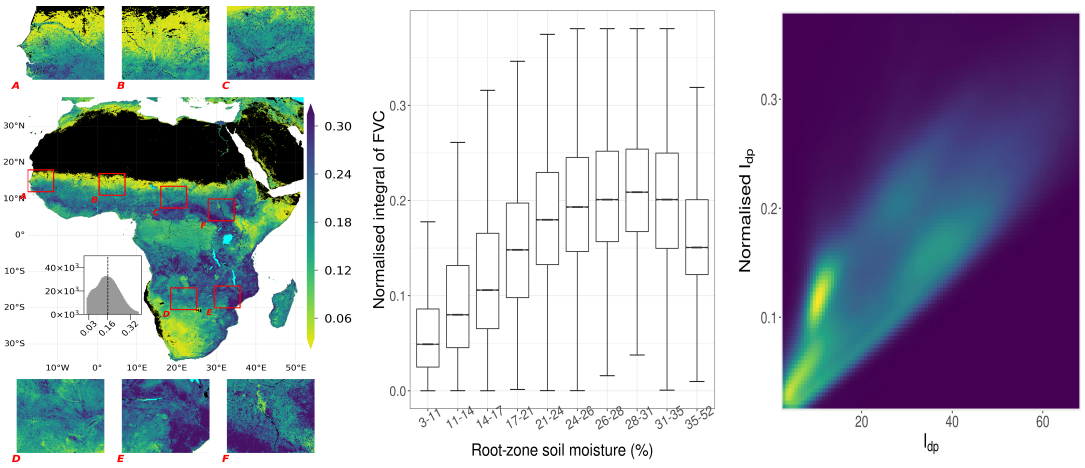

(a) (b) (c)

Figure G1: Integral of FVC time series in the decay period normalised by event duration (a) Spatial variation, (b) variation against within mean annual soil moisture (see Fig. 2c for plotting details). (c) density plot against I_{dp}

Appendix H Map of Number of Convergences of Algorithm 2

Appendix I Maps of Accessible Water Storage Capacity Datasets

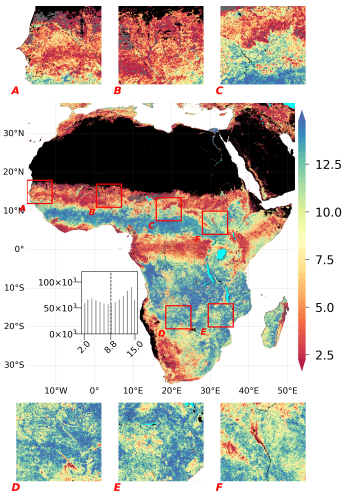

Figure H1: Number of decay periods in which the Algorithm 2 successfully converged.

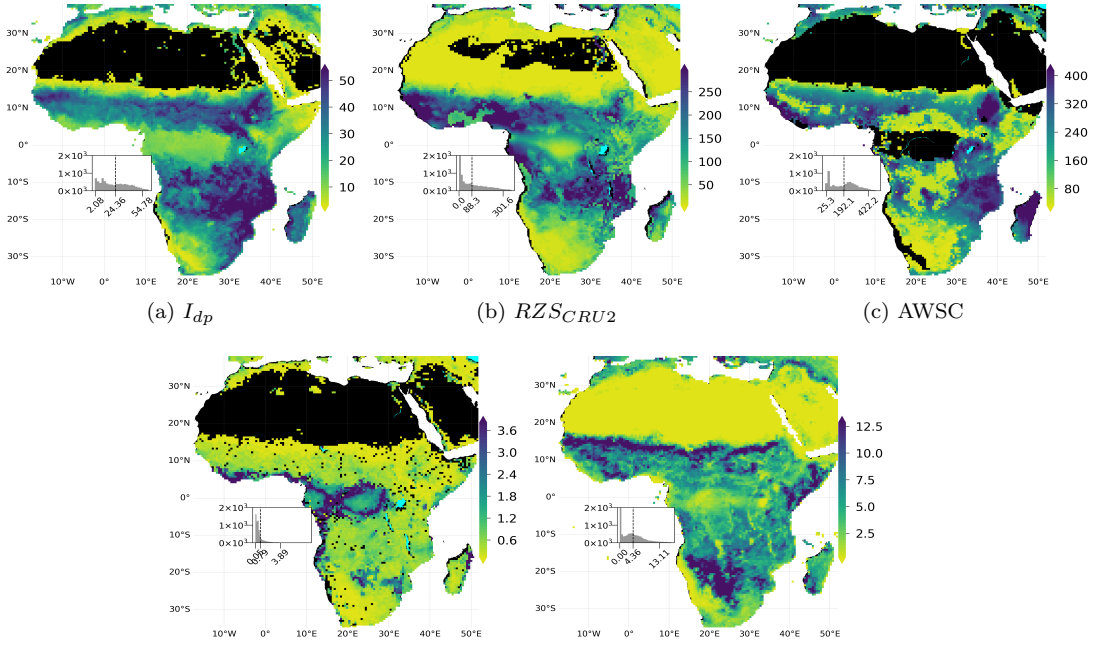

(a) I_{dp} (b) RZS_{CRU2} (c) AWSC

(d) ERD (e) RD

Figure I1: Maps of accessible water storage capacity and rooting depth datasets used in this study. (a) Integral of FVC during decay period, I_{dp}, (b) Root Zone Storage Capacity (RZS_{CRU2}) using CRU as precipitation forcing data with 2 years of drought return period from Wang-Erlandsson et al. (2016), (c) Accessible Water Storage Capacity (AWSC) from S. Tian et al. (2019) (d) Effective Rooting Depth (ERD) from Yang et al. (2016), (e) Rooting Depth (RD) from Fan et al. (2017). All products are aggregated to 0.5° and cropped for the study domain.

References

Adole, T., Dash, J., & Atkinson, P. M. (2016). A systematic review of vegetation phenology in Africa. *Ecological Informatics*, *34*, 117–128. doi: 10.1016/j.ecoinf.2016.05.004

Adole, T., Dash, J., Rodriguez-Galiano, V., & Atkinson, P. M. (2019). Photoperiod controls vegetation phenology across Africa. *Communications Biology*, *2*(1). doi: 10.1038/s42003-019-0636-7

Akasheh, O. Z., Neale, C. M., & Jayanthi, H. (2008). Detailed mapping of riparian vegetation in the middle Rio Grande River using high resolution multi-spectral airborne remote sensing. *Journal of Arid Environments*, *72*(9), 1734–1744. doi: 10.1016/j.jaridenv.2008.03.014

Amatulli, G., McInerney, D., Sethi, T., Strobl, P., & Domisch, S. (2020). Geomorpho90m, empirical evaluation and accuracy assessment of global high-resolution geomorphometric layers. *Scientific Data*, *7*(1), 1–18. doi: 10.1038/s41597-020-0479-6

Anderegg, W. R., Konings, A. G., Trugman, A. T., Yu, K., Bowling, D. R., Gabbitas, R., ... Zenes, N. (2018). Hydraulic diversity of forests regulates ecosystem resilience during drought. *Nature*, *561*(7724), 538–541. doi: 10.1038/s41586-018-0539-7

Barron, O. V., Emelyanova, I., Van Niel, T. G., Pollock, D., & Hodgson, G. (2014). Mapping groundwater-dependent ecosystems using remote sensing measures of vegetation and moisture dynamics. *Hydrological Processes*, *28*(2), 372–385. doi: 10.1002/hyp.9609

Beck, P. S. A., Atzberger, C., Høgda, K. A., Johansen, B., & Skidmore, A. K. (2006). Improved monitoring of vegetation dynamics at very high latitudes: A new method using MODIS NDVI. *Remote Sensing of Environment*, *100*(3), 321–334. doi: 10.1016/j.rse.2005.10.021

Boese, S., Jung, M., Carvalhais, N., Teuling, A. J., & Reichstein, M. (2019). Carbon-water flux coupling under progressive drought. *Biogeosciences*, *16*(13), 2557–2572. doi: 10.5194/bg-16-2557-2019

Caylor, K. K., Manfreda, S., & Rodriguez-Iturbe, I. (2005). On the coupled geomorphological and ecohydrological organization of river basins. *Advances in Water Resources*, *28*(1), 69–86. doi: 10.1016/j.advwatres.2004.08.013

Caylor, K. K., Scanlon, T. M., & Rodríguez-Iturbe, I. (2009). Ecohydrological optimization of pattern and processes in water-limited ecosystems: A trade-off-based hypothesis. *Water Resources Research*, *45*(8), 1–15. doi: 10.1029/2008WR007230

Clark, M. P., Fan, Y., Lawrence, D. M., Adam, J. C., Bolster, D., Gochis, D. J., ... Zeng, X. (2015). Improving the representation of hydrologic processes in Earth System Models. *Water Resources Research*, *51*(8), 5929–5956. doi: 10.1002/2015WR017096

Cronberg, G., Gieske, A., Martins, E., Prince Nengu, J., & Stenström, I.-M. (1995). Hydrobiological studies of the Okavango Delta and Kwando/Linyati/Chobe River, Botswana I surface water quality analysis. *Botswana Notes and Records*, *27*. Retrieved from `http://www.jstor.org/stable/40980045`

Dimiceli, C., Carroll, M., Sohlberg, R., Kim, D. H., Kelly, M., & Townshend, J. R. G. (2015). *MOD44B MODIS/Terra Vegetation Continuous Fields Yearly L3 Global 250m SIN Grid V006.* NASA EOSDIS Land Processes DAAC. doi: 10.5067/MODIS/MOD44B.006

D'Odorico, P., Porporato, A., & Runyan, C. W. (2019). *Dryland ecohydrology.* Springer International Publishing. doi: 10.1007/978-3-030-23269-6

Eamus, D., Zolfaghar, S., Villalobos-Vega, R., Cleverly, J., & Huete, A. (2015). Groundwater-dependent ecosystems: Recent insights from satellite and field-based studies. *Hydrology and Earth System Sciences*, *19*(10), 4229–4256. doi: 10.5194/hess-19-4229-2015

Elzhov, T. V., Mullen, K. M., Spiess, A.-N., & Bolker, B. (2016). minpack.lm: R Interface to the Levenberg-Marquardt Nonlinear Least-Squares Algorithm Found in MINPACK, Plus Support for Bounds [Computer software manual]. Retrieved from `https://cran.r-project.org/package=minpack.lm`

Epstein, H. E., Lauenroth, W. K., & Burke, I. C. (1997). Effects of temperature and soil texture on ANPP in the U.S. Great plains. *Ecology*, *78*(8), 2628–2631. doi: 10.2307/2265921

Everitt, J. H., & Deloach, C. J. (1990). Remote sensing of chinese tamarisk (tamarix chinensis) and associated vegetation. *Weed Science*, *38*(3), 273278. doi: 10.1017/S0043174500056526

Everitt, J. H., Judd, F. W., Escobar, D. E., Alaniz, M. A., Davis, M. R., & Macwhorter, W. (1996). Using remote sensing and spatial information technologies to map sabal palm in the lower Rio Grande Valley of Texas. *Southwestern Naturalist*, *41*(3), 218–226. Retrieved from `http://www.jstor.org/stable/30055117`

Fan, Y., Clark, M., Lawrence, D. M., Swenson, S., Band, L. E., Brantley, S. L., ... Yamazaki, D. (2019). Hillslope hydrology in global change research and earth system modeling. *Water Resources Research*, 1737–1772. doi: 10.1029/2018WR023903

Fan, Y., Miguez-Macho, G., Jobbágy, E. G., Jackson, R. B., & Otero-Casal, C. (2017). Hydrologic regulation of plant rooting depth. *Proceedings of the National Academy of Sciences*, *114*(40), 10572–10577. doi: 10.1073/pnas.1712381114

Fernandez-Illescas, C. P., Porporato, A., Laio, F., & Rodríguez-Iturbe, I. (2001). The ecohydrological role of soil texture in a water-limited ecosystem. *Water Resources Research*, *37*(12), 2863–2872. doi: 10.1029/2000WR000121

Fisher, R. A., & Koven, C. D. (2020). Perspectives on the future of Land Surface Models and the challenges of representing complex terrestrial systems. *Journal of Advances in Modeling Earth Systems*. doi: 10.1029/2018ms001453

GDAL/OGR contributors. (2020). GDAL/OGR geospatial data abstraction software library [Computer software manual]. Retrieved from `https://gdal.org`

Gentine, P., D'Odorico, P., Lintner, B. R., Sivandran, G., & Salvucci, G. (2012). Interdependence of climate, soil, and vegetation as constrained by the Budyko curve. *Geophysical Research Letters*, *39*(19), 2–7. doi: 10.1029/2012GL053492

Gond, V., Fayolle, A., Pennec, A., Cornu, G., Mayaux, P., Camberlin, P., ... Gourlet-Fleury, S. (2013). Vegetation structure and greenness in Central Africa from Modis multi-temporal data. *Philosophical Transactions of the Royal Society B: Biological Sciences*, *368*(1625). doi: 10.1098/rstb.2012.0309

Guan, K., Medvigy, D., Wood, E. F., Caylor, K. K., Li, S., & Jeong, S. J. (2014). Deriving vegetation phenological time and trajectory information over Africa using SEVIRI daily LAI. *IEEE Transactions on Geoscience and Remote Sensing*, *52*(2), 1113–1130. doi: 10.1109/TGRS.2013.2247611

Guan, K., Pan, M., Li, H., Wolf, A., Wu, J., Medvigy, D., ... Lyapustin, A. I. (2015). Photosynthetic seasonality of global tropical forests constrained by hydroclimate. *Nature Geoscience*, *8*(4), 284–289. doi: 10.1038/ngeo2382

Guan, K., Wolf, A., Medvigy, D., Caylor, K. K., Pan, M., & Wood, E. F. (2013). Seasonal coupling of canopy structure and function in African tropical forests and its environmental controls. *Ecosphere*, *4*(3), 1–21. doi: 10.1890/ES12-00232.1

Guan, K., Wood, E. F., Medvigy, D., Kimball, J., Pan, M., Caylor, K. K., ... Jones, M. O. (2014). Terrestrial hydrological controls on land surface phenology of African savannas and woodlands. *Journal of Geophysical Research: Biogeosciences*, *119*(8), 1652-1669. doi: 10.1002/2013JG002572

Guswa, A. J. (2008). The influence of climate on root depth: A carbon cost-

benefit analysis. *Water Resources Research*, *44*(2), 1–11. doi: 10.1029/2007WR006384

Guswa, A. J. (2010). Effect of plant uptake strategy on the water-optimal root depth. *Water Resources Research*, *46*(9), 1–5. doi: 10.1029/2010WR009122

Harris, I., Jones, P. D., Osborn, T. J., & Lister, D. H. (2014). Updated high-resolution grids of monthly climatic observations - the CRU TS3.10 Dataset. *International Journal of Climatology*, *34*(3), 623–642. doi: 10.1002/joc.3711

Hengl, T., Mendes de Jesus, J., Heuvelink, G. B., Gonzalez, M. R., Kilibarda, M., Blagotić, A., ... Kempen, B. (2017). SoilGrids250m: Global gridded soil information based on machine learning. *PLoS ONE*, *12*(2), 1–40. doi: 10.1371/journal.pone.0169748

Herrmann, S. M., & Mohr, K. I. (2011). A continental-scale classification of rainfall seasonality regimes in Africa based on gridded precipitation and land surface temperature products. *Journal of Applied Meteorology and Climatology*, *50*(12), 2504–2513. doi: 10.1175/JAMC-D-11-024.1

Howard, J., & Merrifield, M. (2010). Mapping groundwater dependent ecosystems in California. *PLoS ONE*, *5*(6). doi: 10.1371/journal.pone.0011249

Jacobson, P. J., & Jacobson, K. M. (2013). Hydrologic controls of physical and ecological processes in Namib Desert ephemeral rivers: Implications for conservation and management. *Journal of Arid Environments*, *93*, 80–93. doi: 10.1016/j.jaridenv.2012.01.010

Jin, X. M., Schaepman, M. E., Clevers, J. G., Su, Z. B., & Hu, G. C. (2011). Groundwater depth and vegetation in the Ejina area, China. *Arid Land Research and Management*, *25*(2), 194–199. doi: 10.1080/15324982.2011.554953

Kleidon, A., & Heimann, M. (1998). A method of determining rooting depth from a terrestrial biosphere model and its impacts on the global water and carbon cycle. *Global Change Biology*, *4*(3), 275–286. doi: 10.1046/j.1365-2486.1998.00152.x

Koirala, S., Jung, M., Reichstein, M., de Graaf, I. E., Camps-Valls, G., Ichii, K., ... Carvalhais, N. (2017). Global distribution of groundwater-vegetation spatial covariation. *Geophysical Research Letters*, *44*(9), 4134–4142. doi: 10.1002/2017GL072885

Konings, A. G., & Gentine, P. (2017). Global variations in ecosystem-scale isohydricity. *Global Change Biology*, *23*(2), 891–905. doi: 10.1111/gcb.13389

Kuppel, S., Fan, Y., & Jobbágy, E. G. (2017). Seasonal hydrologic buffer on continents: Patterns, drivers and ecological benefits. *Advances in Water Resources*, *102*, 178–187. doi: 10.1016/j.advwatres.2017.01.004

Laio, F., D'Odorico, P., & Ridolfi, L. (2006). An analytical model to relate the vertical root distribution to climate and soil properties. *Geophysical Research Letters*, *33*(18), 1–5. doi: 10.1029/2006GL027331

Laio, F., Porporato, A., Fernandez-Illescas, C. P., & Rodríguez-Iturbe, I. (2001). Plants in water-controlled ecosystems: Active role in hydrologic processes and response to water stress IV. Discussion of real cases. *Advances in Water Resources*, *24*(7), 745–762. doi: 10.1016/S0309-1708(01)00007-0

Liu, Y., Kumar, M., Katul, G. G., & Porporato, A. (2019). Reduced resilience as an early warning signal of forest mortality. *Nature Climate Change*, *9*(11), 880–885. doi: 10.1038/s41558-019-0583-9

Looney, C. E., Sullivan, B. W., Kolb, T. E., Kane, J. M., & Hart, S. C. (2012). Pinyon pine (Pinus edulis) mortality and response to water addition across a three million year substrate age gradient in northern Arizona, USA. *Plant and Soil*, *357*(1), 89–102. doi: 10.1007/s11104-012-1150-6

LSA-SAF. (2016). *Algorithm Theoretical Basis Document for Vegetation parameters (VEGA)* (Tech. Rep.). Retrieved from `https://nextcloud.lsasvcs.ipma.pt/s/8AcY4xKqtAdLxY5`

Ludwig, J. A., Wilcox, B. P., Breshears, D. D., Tongway, D. J., & Imeson, A. C.

(2005). Vegetation patches and runofferosion as interacting ecohydrological processes in semiarid landscapes. *Ecology*, *86*(2), 288-297. doi: 10.1890/03-0569

Lv, J., Wang, X. S., Zhou, Y., Qian, K., Wan, L., Eamus, D., & Tao, Z. (2013). Groundwater-dependent distribution of vegetation in Hailiutu River catchment, a semi-arid region in China. *Ecohydrology*, *6*(1), 142–149. doi: 10.1002/eco.1254

Mansell, M. G., & Hussey, S. W. (2005). An investigation of flows and losses within the alluvial sands of ephemeral rivers in Zimbabwe. *Journal of Hydrology*, *314*(1-4), 192–203. doi: 10.1016/j.jhydrol.2005.03.015

Martens, B., Miralles, D. G., Lievens, H., Van Der Schalie, R., De Jeu, R. A., Fernández-Prieto, D., ... Verhoest, N. E. (2017). GLEAM v3: Satellite-based land evaporation and root-zone soil moisture. *Geoscientific Model Development*, *10*(5), 1903–1925. doi: 10.5194/gmd-10-1903-2017

Martens, C., Hickler, T., Davis-Reddy, C., Engelbrecht, F., Higgins, S. I., von Maltitz, G. P., ... Scheiter, S. (2021). Large uncertainties in future biome changes in Africa call for flexible climate adaptation strategies. *Global Change Biology*, *27*(2), 340–358. doi: 10.1111/gcb.15390

Martínez-de la Torre, A., Blyth, E. M., & Robinson, E. L. (2019). Evaluation of drydown processes in global land surface and hydrological models using flux tower evapotranspiration. *Water*, *11*. doi: 10.3390/w11020356

McCarthy, T. S. (2006). Groundwater in the wetlands of the Okavango Delta, Botswana, and its contribution to the structure and function of the ecosystem. *Journal of Hydrology*, *320*(3-4), 264–282. doi: 10.1016/j.jhydrol.2005.07.045

McColl, K. A., Wang, W., Peng, B., Akbar, R., Short Gianotti, D. J., Lu, H., ... Entekhabi, D. (2017). Global characterization of surface soil moisture drydowns. *Geophysical Research Letters*, *44*(8), 3682–3690. doi: 10.1002/2017GL072819

Merbold, L., Ardö, J., Arneth, A., Scholes, R. J., Nouvellon, Y., De Grandcourt, A., ... Kutsch, W. L. (2009). Precipitation as driver of carbon fluxes in 11 African ecosystems. *Biogeosciences*, *6*(6), 1027–1041. doi: 10.5194/bg-6-1027-2009

Miralles, D. G., Holmes, T. R., De Jeu, R. A., Gash, J. H., Meesters, A. G., & Dolman, A. J. (2011). Global land-surface evaporation estimated from satellite-based observations. *Hydrology and Earth System Sciences*, *15*(2), 453–469. doi: 10.5194/hess-15-453-2011

Moré, J. J. (1978). The Levenberg-Marquardt algorithm: Implementation and Theory. In G. A. Watson (Ed.), *Lecture notes in mathematics* (pp. 105–116). Berlin: Springer-Verlag.

Müller, C., Waha, K., Bondeau, A., & Heinke, J. (2014). Hotspots of climate change impacts in sub-Saharan Africa and implications for adaptation and development. *Global Change Biology*, *20*(8), 2505–2517. doi: 10.1111/gcb.12586

Münch, Z., & Conrad, J. (2007). Remote sensing and GIS based determination of groundwater dependent ecosystems in the Western Cape, South Africa. *Hydrogeology Journal*, *15*(1), 19–28. doi: 10.1007/s10040-006-0125-1

Nash, E., & Sutcliffe, V. (1970). River flow forecasting through conceptual models Part I - A discussion of principles. *Journal of Hydrology*, *10*, 282–290. doi: 10.1016/0022-1694(70)90255-6

Neale, C. M. (1997). Classification and mapping of riparian systems using airborne multispectral videography. *Restoration Ecology*, *5*, 103–112. doi: 10.1111/j.1526-100X.1997.00103.x

Nelson, J. A., Pérez-Priego, O., Zhou, S., Poyatos, R., Zhang, Y., Blanken, P. D., ... Jung, M. (2020). Ecosystem transpiration and evaporation: Insights from three water flux partitioning methods across FLUXNET sites. *Global Change Biology*, *26*(12), 6916–6930. doi: 10.1111/gcb.15314

Newman, B. D., Wilcox, B. P., Archer, S. R., Breshears, D. D., Dahm, C. N., Duffy,

C. J., ... Vivoni, E. R. (2006). Ecohydrology of water-limited environments: A scientific vision. *Water Resources Research*, *42*(6), 1–15. doi: 10.1029/2005WR004141

Nobre, A. D., Cuartas, L. A., Hodnett, M., Rennó, C. D., Rodrigues, G., Silveira, A., ... Saleska, S. (2011). Height Above the Nearest Drainage - a hydrologically relevant new terrain model. *Journal of Hydrology*, *404*(1-2), 13–29. doi: 10.1016/j.jhydrol.2011.03.051

Noy-Meir, I. (1973). Desert ecosystems: Environment and producers. *Annual Review of Ecology and Systematics*, *4*(1), 25-51. doi: 10.1146/annurev.es.04.110173.000325

Ouédraogo, D. Y., Hardy, O. J., Doucet, J. L., Janssens, S. B., Wieringa, J. J., Stoffelen, P., ... Fayolle, A. (2020). Latitudinal shift in the timing of flowering of tree species across tropical Africa: Insights from field observations and herbarium collections. *Journal of Tropical Ecology*. doi: 10.1017/S0266467420000103

Palmer, P. I., Feng, L., Baker, D., Chevallier, F., Bösch, H., & Somkuti, P. (2019). Net carbon emissions from African biosphere dominate pan-tropical atmospheric CO2 signal. *Nature Communications*, *10*(1), 1–9. doi: 10.1038/s41467-019-11097-w

Peñuelas, J., Filella, I., Zhang, X., Llorens, L., Ogaya, R., Lloret, F., ... Terradas, J. (2004). Complex spatiotemporal phenological shifts as a response to rainfall changes. *New Phytologist*, *161*(3), 837–846. doi: 10.1111/j.1469-8137.2004.01003.x

Porporato, A., Laio, F., Ridolfi, L., & Rodríguez-Iturbe, I. (2001). Plants in water-controlled ecosystems: active role in hydrologic processes and response to water stress: Iii. vegetation water stress. *Advances in Water Resources*, *24*(7), 725-744. doi: 10.1016/S0309-1708(01)00006-9

Raduła, M. W., Szymura, T. H., & Szymura, M. (2018). Topographic wetness index explains soil moisture better than bioindication with Ellenberg's indicator values. *Ecological Indicators*, *85*(October 2017), 172–179. doi: 10.1016/j.ecolind.2017.10.011

Rodríguez-Iturbe, I., D'Odorico, P., Porporato, A., & Ridolfi, L. (1999). On the spatial and temporal links between vegetation, climate, and soil moisture. *Water Resources Research*, *35*(12), 3709-3722. doi: 10.1029/1999WR900255

Rousseeuw, P. J., & Croux, C. (1993). Alternatives to the median absolute deviation. *Journal of the American Statistical Association*, *88*(424), 1273–1283. doi: 10.1080/01621459.1993.10476408

Sala, O. E., Parton, W. J., Joyce, L. A., & Lauenroth, W. K. (1988). Primary production of the central grassland region of the United States. *Ecology*, *69*(1), 40–45. doi: 10.2307/1943158

Sankaran, M., Hanan, N. P., Scholes, R. J., Ratnam, J., Augustine, D. J., Cade, B. S., ... Zambatis, N. (2005). Determinants of woody cover in African savannas. *Nature*, *438*(7069), 846–849. doi: 10.1038/nature04070

Sankaran, M., Ratnam, J., & Hanan, N. (2008). Woody cover in African savannas: The role of resources, fire and herbivory. *Global Ecology and Biogeography*, *17*(2), 236–245. doi: 10.1111/j.1466-8238.2007.00360.x

Scanlon, T. M., Caylor, K. K., Manfreda, S., Levin, S. A., & Rodríguez-Iturbe, I. (2005). Dynamic response of grass cover to rainfall variability: Implications for the function and persistence of savanna ecosystems. *Advances in Water Resources*, *28*(3), 291–302. doi: 10.1016/j.advwatres.2004.10.014

Schenk, H. J. (2008). The shallowest possible water extraction profile: A null model for global root distributions. *Vadose Zone Journal*, *7*(3), 1119. doi: 10.2136/vzj2007.0119

Schenk, H. J., & Jackson, R. B. (2002). Rooting depths, lateral root spreads and belowground aboveground allometries of plants in water limited ecosystems.

Journal of Ecology, *90*, 480–494. doi: 10.1046/j.1365-2745.2002.00682.x

Schmiedel, U., Jacke, V., Hachfeld, B., & Oldeland, J. (2021). Response of Kalahari vegetation to seasonal climate and herbivory: Results of 15years of vegetation monitoring. *Journal of Vegetation Science*, *32*(1), 1–13. doi: 10.1111/jvs.12927

Simard, M., Pinto, N., Fisher, J. B., & Baccini, A. (2011). Mapping forest canopy height globally with spaceborne lidar. *Journal of Geophysical Research: Biogeosciences*, *116*(4), 1–12. doi: 10.1029/2011JG001708

Singh, C., Wang-Erlandsson, L., Fetzer, I., Rockström, J., & Van Der Ent, R. (2020). Rootzone storage capacity reveals drought coping strategies along rainforest-savanna transitions. *Environmental Research Letters*, *15*(12). doi: 10.1088/1748-9326/abc377

Tao, S., Guo, Q., Li, C., Wang, Z., & Fang, J. (2016). Global patterns and determinants of forest canopy height. *Ecology*, *97*(12), 3265–3270. doi: 10.1002/ecy.1580

Taylor, R. G., Todd, M. C., Kongola, L., Maurice, L., Nahozya, E., Sanga, H., & Macdonald, A. M. (2013). Evidence of the dependence of groundwater resources on extreme rainfall in East Africa. *Nature Climate Change*, *3*(4), 374–378. doi: 10.1038/nclimate1731

Teuling, A. J., Seneviratne, S. I., Williams, C., & Troch, P. A. (2006). Observed timescales of evapotranspiration response to soil moisture. *Geophysical Research Letters*, *33*(23), 0–4. doi: 10.1029/2006GL028178

Tian, F., Wigneron, J. P., Ciais, P., Chave, J., Ogée, J., Peñuelas, J., ... Fensholt, R. (2018). Coupling of ecosystem-scale plant water storage and leaf phenology observed by satellite. *Nature Ecology and Evolution*, *2*(9), 1428–1435. doi: 10.1038/s41559-018-0630-3

Tian, S., Van Dijk, A. I., Tregoning, P., & Renzullo, L. J. (2019). Forecasting dryland vegetation condition months in advance through satellite data assimilation. *Nature Communications*, *10*(1), 1–7. doi: 10.1038/s41467-019-08403-x

Tootchi, A., Jost, A., & Ducharne, A. (2019). Multi-source global wetland maps combining surface water imagery and groundwater constraints. *Earth System Science Data*, *892657*, 189–220. doi: 10.5194/essd-11-189-2019

Tooth, S. (2000). Process, form and change in dryland rivers: A review of recent research. *Earth Science Reviews*, *51*(1-4), 67–107. doi: 10.1016/S0012-8252(00)00014-3

Trigo, I. F., Dacamara, C. C., Viterbo, P., Roujean, J. L., Olesen, F., Barroso, C., ... Arboleda, A. (2011). The satellite application facility for land surface analysis. *International Journal of Remote Sensing*, *32*(10), 2725–2744. doi: 10.1080/01431161003743199

Tropical Rainfall Measuring Mission (TRMM). (2011). *TRMM (TMPA) Rainfall Estimate L3 V7.* Goddard Earth Sciences Data and Information Services Center (GES DISC). doi: 10.5067/TRMM/TMPA/3H/7

Valentini, R., Arneth, A., Bombelli, A., Castaldi, S., Cazzolla Gatti, R., Chevallier, F., ... Scholes, R. J. (2014). A full greenhouse gases budget of Africa: Synthesis, uncertainties, and vulnerabilities. *Biogeosciences*, *11*(2), 381–407. doi: 10.5194/bg-11-381-2014

van Dijk, A. I., Peña-Arancibia, J. L., Wood, E. F., Sheffield, J., & Beck, H. E. (2013). Global analysis of seasonal streamflow predictability using an ensemble prediction system and observations from 6192 small catchments worldwide. *Water Resources Research*, *49*(5), 2729–2746. doi: 10.1002/wrcr.20251

van Wijk, M. T. (2011). Understanding plant rooting patterns in semi-arid systems: An integrated model analysis of climate, soil type and plant biomass. *Global Ecology and Biogeography*, *20*(2), 331–342. doi: 10.1111/j.1466-8238.2010.00601.x

Wang, J., Song, C., Reager, J. T., Yao, F., Famiglietti, J. S., Sheng, Y., ... Wada,

Y. (2018). Recent global decline in endorheic basin water storages. *Nature Geoscience*, *11*(12), 926–932. doi: 10.1038/s41561-018-0265-7

Wang-Erlandsson, L., Bastiaanssen, W. G., Gao, H., Jägermeyr, J., Senay, G. B., Van Dijk, A. I., ... Savenije, H. H. (2016). Global root zone storage capacity from satellite-based evaporation. *Hydrology and Earth System Sciences*, *20*(4), 1459–1481. doi: 10.5194/hess-20-1459-2016

Weber, U., Jung, M., Reichstein, M., Beer, C., Braakhekke, M., Lehsten, V., ... Ciais, P. (2009). The inter-annual variability of Africa's ecosystem productivity: a multi-model analysis. *Biogeosciences*, *6*, 285–295. doi: 10.5194/bg-6-285-2009

Weerasinghe, I., Bastiaanssen, W., Mul, M., Jia, L., & Van Griensven, A. (2020). Can we trust remote sensing evapotranspiration products over Africa. *Hydrology and Earth System Sciences*, *24*(3), 1565–1586. doi: 10.5194/hess-24-1565-2020

Wei, F., Wang, S., Fu, B., Wang, L., Liu, Y. Y., & Li, Y. (2019). African dryland ecosystem changes controlled by soil water. *Land Degradation and Development*, *30*(13), 1564–1573. doi: 10.1002/ldr.3342

Wei, Z., Yoshimura, K., Wang, L., Miralles, D. G., Jasechko, S., & Lee, X. (2017). Revisiting the contribution of transpiration to global terrestrial evapotranspiration. *Geophysical Research Letters*, *44*(6), 2792–2801. doi: 10.1002/2016GL072235

Wilcox, B. P., Le Maitre, D., Jobbagy, E., Wang, L., & Breshears, D. D. (2017). Ecohydrology: Processes and implications for rangelands. In D. D. Briske (Ed.), *Rangeland systems: Processes, management and challenges* (pp. 85–129). Springer International Publishing. doi: 10.1007/978-3-319-46709-2_3

Williams, C. A., & Albertson, J. D. (2004). Soil moisture controls on canopy-scale water and carbon fluxes in an African savanna. *Water Resources Research*, *40*(9), 1–14. doi: 10.1029/2004WR003208

Williams, C. A., Hanan, N. P., Neff, J. C., Scholes, R. J., Berry, J. A., Denning, A. S., & Baker, D. F. (2007). Africa and the global carbon cycle. *Carbon Balance and Management*, *2*(1). doi: 10.1186/1750-0680-2-3

Xu, X., Medvigy, D., Powers, J. S., Becknell, J. M., & Guan, K. (2016). Diversity in plant hydraulic traits explains seasonal and inter-annual variations of vegetation dynamics in seasonally dry tropical forests. *New Phytologist*, *212*(1), 80–95. doi: 10.1111/nph.14009

Yamazaki, D., Ikeshima, D., Sosa, J., Bates, P. D., Allen, G. H., & Pavelsky, T. M. (2019). MERIT Hydro: A high-resolution global hydrography map based on latest topography dataset. *Water Resources Research*, *55*(6), 5053–5073. doi: 10.1029/2019WR024873

Yan, D., Zhang, X., Yu, Y., & Guo, W. (2016). A comparison of tropical rainforest phenology retrieved from geostationary (SEVIRI) and polar-orbiting (MODIS) sensors across the Congo Basin. *IEEE Transactions on Geoscience and Remote Sensing*, *54*(8), 4867–4881. doi: 10.1109/TGRS.2016.2552462

Yan, D., Zhang, X., Yu, Y., & Guo, W. (2017). Characterizing land cover impacts on the responses of land surface phenology to the rainy season in the Congo Basin. *Remote Sensing*, *9*(5). doi: 10.3390/rs9050461

Yang, Y., Donohue, R. J., & McVicar, T. R. (2016). Global estimation of effective plant rooting depth: Implications for hydrological modeling. *Water Resources Research*, *52*, 8260–8276. doi: 10.1111/j.1752-1688.1969.tb04897.x

Zeng, L., Wardlow, B. D., Xiang, D., Hu, S., & Li, D. (2020). A review of vegetation phenological metrics extraction using time-series, multispectral satellite data. *Remote Sensing of Environment*, *237*, 111511. doi: 10.1016/j.rse.2019.111511

Zhang, J., Felzer, B. S., & Troy, T. J. (2016). Extreme precipitation drives groundwater recharge: the Northern High Plains Aquifer, central United States, 19502010. *Hydrological Processes*, *30*(14), 2533–2545. doi: 10.1002/hyp.10809

Zhang, W., Brandt, M., Penuelas, J., Guichard, F., Tong, X., Tian, F., & Fensholt, R. (2019). Ecosystem structural changes controlled by altered rainfall climatology in tropical savannas. *Nature Communications*, *10*(1). doi: 10.1038/s41467-019-08602-6

Zimba, H., Kawawa, B., Chabala, A., Phiri, W., Selsam, P., Meinhardt, M., & Nyambe, I. (2018). Assessment of trends in inundation extent in the Barotse Floodplain, upper Zambezi River Basin: A remote sensing-based approach. *Journal of Hydrology: Regional Studies*, *15*(January), 149–170. doi: 10.1016/j.ejrh.2018.01.002